The experimental observation and modeling of an "Ovaici" necklace and stick–spurt instability arising during the cold extrusion of chocolate

H. Ovaici and M. R. Mackley[a)]

Department of Chemical Engineering, University of Cambridge, Cambridge, CB2 3RA, United Kingdom

G. H. McKinley

Division of Engineering and Applied Sciences, Harvard University, Cambridge, Massachusetts 02138

S. J. Crook

Department of Chemical Engineering, University of Cambridge, Cambridge, CB2 3RA, United Kingdom

(Received 19 June 1997; final revision received 6 October 1997)

Synopsis

This paper reports experimental results and modeling relating to the ambient temperature, cold extrusion of chocolate. In particular, extrusion conditions are given where two different modes of instability are described and modeled. In the first case, at low flow rates, a stick–spurt instability is observed, which leads to large amplitude fluctuations in the extrusion pressure and extrudate velocity. This instability is modeled as a modified relaxation oscillation process in which the combined nonlinear plastic flow behavior of the chocolate and the compressibility of the material in the reservoir control the instability mechanism. The second mode of instability, observed for a specific thermal history, concerns the unusual extrusion of a ''necklace'' structure consisting of beads regularly spaced on a narrow extrudate core. This instability is explained in terms of the steady core–annular coextrusion of two Bingham-plastic chocolate components having different yield stresses. © *1998 The Society of Rheology.* [S0148-6055(98)00701-9]

I. INTRODUCTION

The cold extrusion of solid chocolate is a recently discovered process in which chocolate can be cold formed via plastic deformation at temperatures below the material's peak melting point [Beckett *et al.* (1994)]. The process is nominally isothermal, although local adiabatic heating via compression or viscous heating may be important. The product is shape retaining with a level of temporary flexibility enabling, for example, an extruded filament of chocolate to be tied in knots immediately after extrusion. The pressure-driven extrusion is essentially a plastic flow process with extrusion pressures typically varying in

a)Corresponding author.

the range 10–300 bar, depending on extruder barrel and extrusion die geometry, in a temperature range of 25–5 °C. Hereafter, we refer to this process as the ''cold extrusion of chocolate.''

During the course of experiments carried out on the cold extrusion process, we observed two different and quite striking forms of extrusion instabilities, and the purpose of this paper is to describe these instabilities and also model their behavior using simple but physically realistic assumptions. We believe the mechanisms used in this paper to describe these instabilities may be relevant to extrusion instabilities observed in other non-Newtonian materials.

The subject of extrusion instabilities for a range of materials has been considered by a number of authors. By far the most published work has been for polymer systems where the onset of extrusion instabilities can limit the throughput of the process. A review by Larson (1992) and papers by Sornberger *et al.* (1987), Petrie and Denn (1976), and Benbow and Lamb (1963) cover experimental observations and attempt to model the mechanism for instability. Recent literature on gross extrudate distortion includes Piau *et al.* (1995) and Becker *et al.* (1991) while papers on smaller scale ''sharkskin'' instabilities are covered by Piau *et al.* (1995), Firdaus and Tong (1992), and Beaufils *et al.* (1989). There are many postulated phenomenological explanations for the origin of polymer instabilities [Larson (1992)] ranging from relaxation oscillation models [Molenaar and Koopmans (1994); Weill (1980)], stick–slip explanations [Adewale *et al.* (1991); Adewale and Leonov (1993); Georgiou and Crochet (1994a) (1994b); Wang and Drda (1996)], and nonlinear constitutive responses [Pearson (1994); Kolkka *et al.* (1988)]. There appear to be fewer recorded observations of extrusion instabilities for materials that flow in a plastic manner or exhibit a yield stress. Benbow and Bridgwater (1993) review some extrusion instabilities seen for certain ceramic pastes, however, by comparison with polymeric materials, the onset of these instabilities appears to be rare.

This paper is divided into three main sections followed by a discussion and conclusion. In the first section, the general cold extrusion characteristics of chocolate are summarized. The effect of extrusion temperature and chocolate composition is explored together with the way the extrusion pressure depends both on time and the imposed extrusion flow rate. In the second section, the stick–spurt instability is described and modeled using data from the first section and a modified form of relaxation–oscillation theory suitable for a compressible viscoplastic material. The third section describes the experimental conditions and thermal history required in order to observe the ''Ovaici necklace,'' and the characteristics of this necklace extrusion is explained using a model in which the chocolate is treated as a two-component Bingham-plastic material that is co-extruded in a core–annular configuration.

II. STEADY FLOW COLD EXTRUSION

The majority of the cold extrusion experiments described in this paper were carried out using a modified piston-driven Davenport rheometer. A schematic diagram of the apparatus is shown in Fig. 1. An extrusion die is held at the bottom of a two-piece barrel that is temperature controlled by circulation of a water/glycol mixture and we estimate the temperature control within the barrel and die to be of the order ± 0.2 °C. The piston can be advanced at a preset piston speed U_p (corresponding to a flow rate $Q_i = U_p A_p$ where A_p is the area of the piston) and the extrusion pressure is measured using a 1–700 bar transducer mounted into the sidewall of the barrel positioned upstream of the die. In order to achieve high extrusion rates, some experiments were carried out using a modified Betol–Manumold injection moulding unit. In this case, a pressure-driven ram drove the

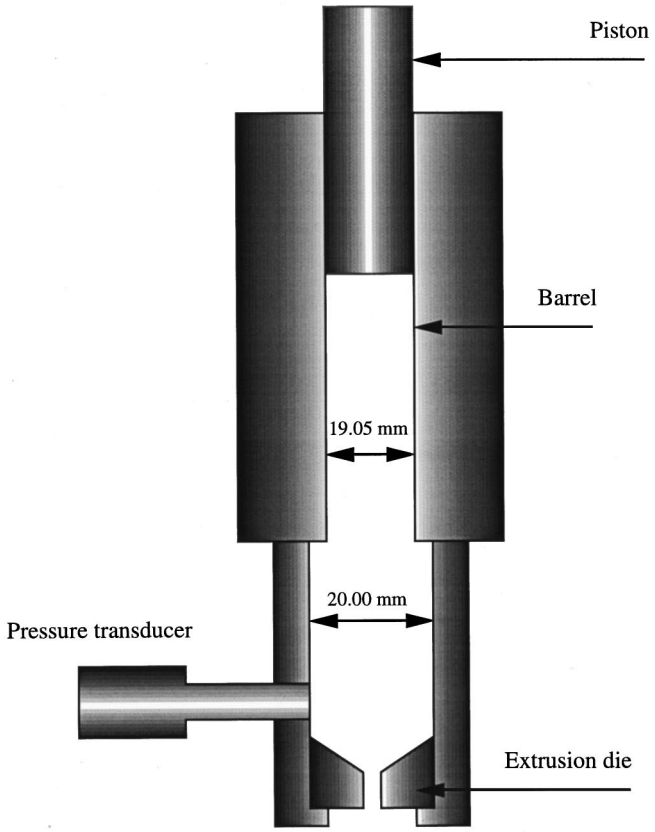

FIG. 1. Schematic diagram of the Davenport rheometer.

chocolate into the same extrusion die that was used with the Davenport. The steady flow data described in this section were obtained using a stainless-steel die of die-land length $L = 4$ mm, internal diameter $D = 4$ mm, and entry angle $\phi = 45°$. Henceforth, we denote these conditions in the form $L/D/\phi$.

Two chocolate compositions (milk and plain) were used in the experiments described here and, unless stated otherwise, both chocolates had been melt tempered by the manufacturer and solidified in the normal way. The approximate compositions of the milk and plain chocolate used are given in Table I, together with the initial size of the individual solid chocolate pieces.

TABLE I. Properties of chocolate.

	Milk	Plain
Mass fraction of sugar crystals	0.45	0.50
Mass fraction of cocoa solids	0.06	0.20
Mass fraction of cocoa butter	0.20	0.27
Mass fraction of milk fat	0.08	0.02
Mass fraction of milk solids	0.18	none
Mass fraction of other components	0.03	0.01
Mean particle size of sugar crystals	18 μm	18 μm
Mean size of chocolate pieces	3000 μm	3000 μm

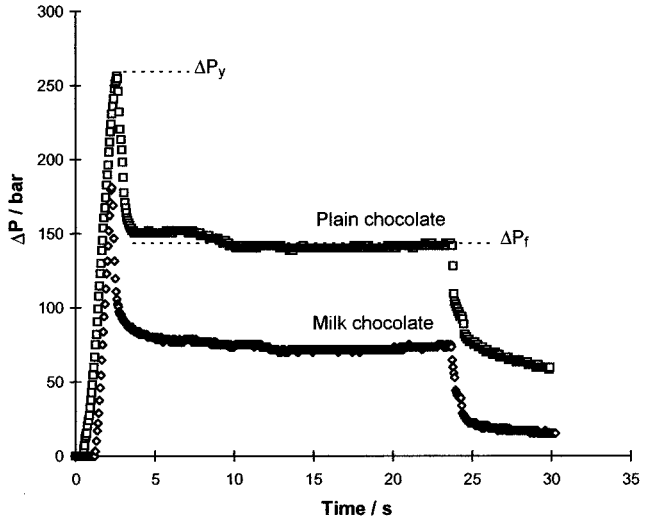

FIG. 2. General extrusion characteristics. Pressure difference as a function of time for the cold extrusion of plain and milk chocolate: $T = 20\,^{\circ}\mathrm{C}$, Q (using Manumold) $= 1.608\times10^{-6}$ m^3/s, and die = 4/4/45°. Piston cessation after 24 s. (□) = plain chocolate, and (◇) = milk chocolate. ΔP_y corresponds to yield pressure, and ΔP_f corresponds to mean flow pressure.

A typical experiment involves charging the barrel with chocolate pieces, allowing the chocolate to thermally equilibrate to the required temperature, and then monitoring the extrusion pressure as a function of time for a set piston speed. Typical data for both plain and milk chocolate are shown in Fig. 2. The plain chocolate requires significantly higher extrusion pressures than the milk chocolate, which could be explained by the lower amount of milk fat in the chocolate. This is a feature of interest but is not examined further in this paper. In both cases, the extrusion profiles follow a similar form. After an initial compaction period, the extrusion pressure passes through a peak that we identify as a yield pressure ΔP_y. When the flow has become fully established, the pressure drops and reaches a plateau flow value ΔP_f, which to a first approximation is usually independent of piston position. At the cessation of the flow, which occurs in Fig. 2 after 24 s, there is usually a sharp drop in pressure followed by a subsequent viscoplastic relaxation. From flow visualization studies we have established that under steady flow conditions the chocolate appears to exhibit slip in a narrow boundary layer adjacent to the wall at least in the parallel section of the extrusion die [Crook (1997)].

The yield pressure ΔP_y and the flow pressure ΔP_f are both sensitive functions of the die geometry in addition to the chocolate composition and temperature. The overall constitutive response for milk chocolate in cold extrusion through a 4/4/45° die is shown in Fig. 3 in the form of a time-averaged or steady flow curve. Here, the measured extrusion pressure is shown as a function of the piston flow rate for three different extrusion temperatures. In each case, it can be seen that the extrusion pressure appears to start from a yield value and then decreases with increasing flow rate before subsequently showing a moderate increase with flow rate. The extrusion pressure is very sensitive to temperature and decreases approximately linearly with temperature in the temperature window tested. The fitting of the measured extrusion pressure–flow-rate data to an appropriate constitutive model is described in the following section.

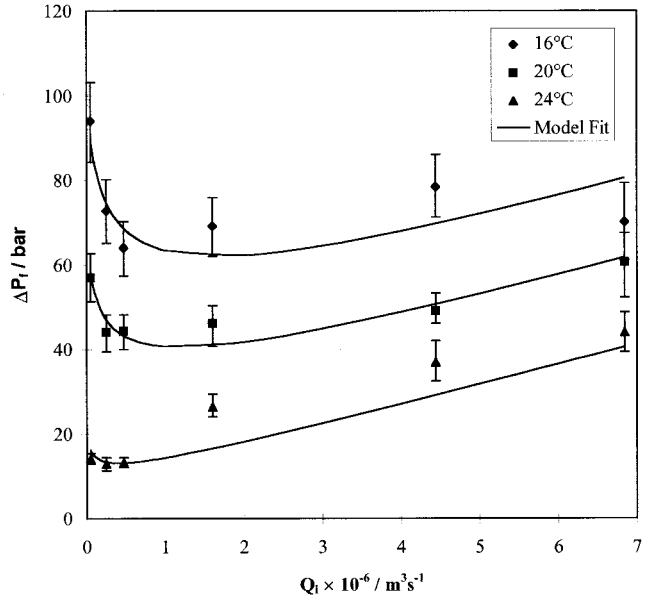

FIG. 3. The effect of input flow rate on mean flow pressure ΔP_f. Graph of mean flow pressure as a function of steady flow rate for milk chocolate at three different extrusion temperatures. $T = 16\,^{\circ}\mathrm{C}$ (closed diamonds), 20 °C (closed squares), and 24 °C (closed triangles). Die = 4/4/45°. Maximum and minimum pressures for each extrusion experiment indicated by vertical bars. The solid lines are the regression to the experimental data as given by Eq. (3.3).

III. THE STICK–SPURT EXTRUSION INSTABILITY

Under certain processing conditions, steady operation of cold extrusion is not possible and we observe a transition to a new flow regime characterized by a stick–spurt flow instability. The onset of instability is generally observed at low flow rates in our experiments and also at lower processing temperatures.

A. Experimental observations

An example of the unsteady flow is shown in Fig. 4. The experimental protocol is the same as that described in Sec. II, and in this case, a die of die-land length $L = 32$ mm was used. When the piston of the rheometer was advanced at a constant speed of 10 mm/min and at an extrusion temperature of 16 °C, a classic ''stick–spurt'' extrusion instability was observed. Figure 4 shows the time evolution of both the pressure and extrudate velocity fluctuations for a milk chocolate. The extrudate velocity was determined from video sequences of the displacement of the extrudate as it emerged from the extrusion die. Figure 4 shows that approximately every six seconds there is a ''spurt'' in which chocolate is rapidly extruded from the die. Between these spurts, there are periods when no chocolate emerges although the piston in the barrel continues to advance at a constant velocity. When the extrudate does flow, its extruded diameter is slightly undersized compared to the diameter of the extrusion die. There is no die swell and the material possesses temporary flexibility as described previously. Figure 4 also shows the coupled pressure oscillation that is associated with the stick–spurt event. At the instant before a spurt, the pressure reaches a maximum value. Immediately flow starts, and the pressure drops rapidly to a lower value. During the period of flow cessation, the pressure then steadily builds again linearly in time until an identical maximum value is reattained,

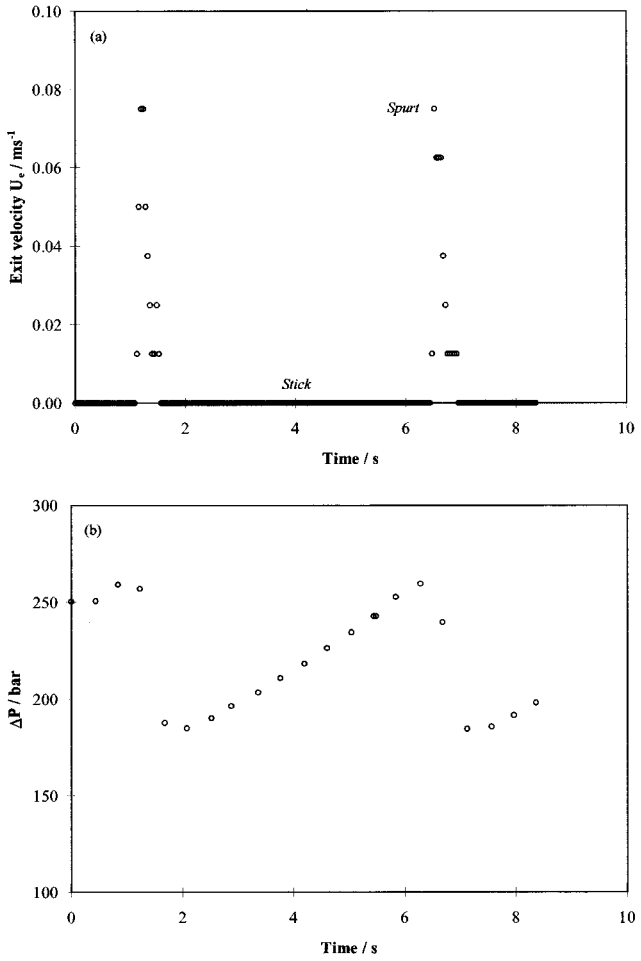

FIG. 4. Stick–spurt oscillations in the cold extrusion of milk chocolate at 16 °C through a 32/4/45° die. Flow rate is 5.0×10^{-8} m^3/s. (a) Time evolution of extrudate velocity, and (b) Time evolution of extrusion pressure. Both the velocity and pressure fluctuations are coupled in phase and exhibit repeated oscillations with a period of approximately 6 s.

and the stick–spurt cycle repeats again in a time-periodic manner. Both the velocity and pressure fluctuations are of a large magnitude and are coupled in phase.

B. Modeling of the stick–spurt instability

The modeling of the stick–slip instabilities and spurt oscillations commonly observed in polyolefin melts at elevated temperatures invokes the existence of local maxima in the ''flow curve'' describing the pressure-difference–flow-rate relationship for the particular geometry of interest [Pearson (1994)]. The physical mechanisms leading to this non-monotonicity are not always clear but are commonly taken to be either (a) inherent to the constitutive relationship for describing the stress versus strain-rate in the material [e.g., Kolkka *et al.* (1988); Malkus *et al.* (1990)], or (b) related to a nonlinear static frictional model for the slip velocity [e.g., Georgiou and Crochet (1994a)(1994b)] or a dynamical slip model [e.g., Graham (1995)]. The nonmonotonic flow curves lead to the onset of

''constitutive instabilities'' or ''material instabilities'' [Larson (1992); Goddard (1996)], which result in large-amplitude nonlinear oscillations of the pressure and/or flow rate.

1. Rheological modeling

A general tensorial constitutive relationship describing the state of stress and strain rate in deforming chocolate is not currently available, however, it is apparent that a number of phenomenological observations must be incorporated, for example; (i) the material exhibits a viscoplastic response with an apparent yield point at elevated pressures; (ii) the material parameters are sensitive functions of the temperature, T, and the composition of the chocolate; and (iii) the viscous contribution to the stress is much smaller than the plastic contribution. Chevalley (1975) states that in the molten state, the chocolate can be modeled using the Herschel–Bulkley constitutive model, and other constitutive relationships are suggested by Holdsworth (1993).

The simplest appropriate constitutive relationship capturing the experimental observations at low temperatures and elevated pressures is the generalized Bingham plastic relationship

$$\begin{aligned} \dot{\boldsymbol{\gamma}} &= 0, \quad \tau < \tau_y, \\ \boldsymbol{\tau} &= \eta(\dot{\gamma})\dot{\boldsymbol{\gamma}}, \quad \dot{\gamma} \geqslant 0, \end{aligned} \tag{3.1}$$

where $|\boldsymbol{\tau}| = \tau$, $|\dot{\boldsymbol{\gamma}}| = \dot{\gamma}$, and

$$\eta(\dot{\gamma}) = \left[\frac{\tau_y(T,C)+\mu(T,C)\dot{\gamma}}{\dot{\gamma}}\right]. \tag{3.2}$$

Here, τ_y is the yield stress and μ the viscosity of the material, which both may be (different) functions of temperature T, and material composition, denoted generically by the variable C.

Numerical solution of Eqs. (3.1) and (3.2) for a particular material at a given temperature in a specific extruder geometry can lead to a flow curve $\Delta P_f(Q_e)$ relating the steady or time-averaged extrusion pressure ΔP_f to the extrudate flow rate Q_e. Although we do not have the precise form of the expressions for τ_y and μ, we are able to observe the resulting flow curve for the die geometries employed in the Davenport extruder (cf. Fig. 3). It is clear from these experimental observations that at low temperatures the flow curve is nonmonotonic with a local minimum at low imposed piston velocities $U_{\mathrm{p}} = Q_i/A_{\mathrm{p}}$. A suitable empirical relationship for modeling these data is

$$\Delta P_f = \frac{\Delta P_y}{(1+bQ_e)^n} + \bar{\mu}Q_e, \quad \text{for } Q_e \geqslant 0, \tag{3.3}$$

where ΔP_y, b, n, and $\bar{\mu}$ are model parameters that are functions of T and C and can be determined by regression to the flow curve data. Here, ΔP_y is the yield pressure for flow and is related to the yield stress τ_y of the material. The parameter $\bar{\mu}$ is the apparent viscous contribution to the pressure difference and depends on the viscosity $\mu(T,C)$ and the aspect ratio L/D of the die. Typical values for the material parameters are given in Tables II and III, and the regression to the data is shown in Fig. 3 for milk chocolate and temperatures in the range $16 \leqslant T \leqslant 24$ °C for a 4/4/45° die. It can be observed that the model parameters for the milk chocolate at 20 °C for a 4/4/45° die in Tables II and III are different. The model parameters in Table II were obtained by regression to the experimental flow curve data in Fig. 3, where each data point is the average of many experi-

TABLE II. Material parameters for the steady flow curves $\Delta P_s(Q_e)$ given by Eq. (3.3) describing the cold extrusion of chocolate in dies of varying dimensions at different ambient temperatures.

Material	Milk	Milk	Milk
Temperature	16 °C	20 °C	24 °C
Die	4/4/45°	4/4/45°	4/4/45°
Flow curve parameters			
ΔP_y(bar)	100	70	20
b (s/m^3)	15×10^6	30×10^6	45×10^6
n (−)	1/5	1/5	1/5
$\bar{\mu}$ (bar s/m^3)	6×10^6	5.5×10^6	5×10^6

ments, whereas the model parameters in Table III were derived for a single extrusion experiment only. The experiments were also carried out in different extruders, and different batches of chocolate were used.

The curves given by the chosen form of the constitutive relationship have a negative slope at $Q_e = 0$ if $(-nb\Delta P_y + \bar{\mu}) < 0$ and the flow curve exhibits a local minimum in the steady extrusion pressure at a flow rate

$$Q_{\min} = \frac{\bar{\mu}}{\Delta P_y nb},$$

plus an associated local minimum in the steady extrusion pressure $\Delta P_{\min} = \Delta P_f(Q_{\min})$. As we show below, crosshead speeds corresponding to $Q_i < Q_{\min}$ are unstable and lead to large amplitude pressure fluctuations and a stick–slip flow. At higher temperatures ($T \geqslant 24\,°\mathrm{C}$), the yield pressure decreases rapidly as the chocolate softens, and the material behaves more like a viscous liquid with a very small yield stress.

Photographic and video observations of the chocolate deformation within the converging region of the extruder and the die-land indicate that the motion is, to a first approximation, one-dimensional with a thin sliplike layer of yielded and deforming chocolate near the wall of the die, which also extends axially upwards above the die entrance forming an interior yield surface within the barrel. Within this cylindrical yield surface, the central core undergoes plug flow. Similar flow patterns have been predicted in numerical calculations in entry flows of Bingham plastics near 90° abrupt contractions [Papanastasiou (1987)]. As a result, a one-dimensional analysis of the extrusion process should provide a good approximation to the actual dynamics observed experimentally.

TABLE III. Material parameters for the steady flow curves $\Delta P_s(Q_e)$ given by Eq. (3.3) describing the cold extrusion of chocolate in dies of varying dimensions at different ambient temperatures.

Material	Milk	Plain	Milk
Temperature	20 °C	20 °C	16 °C
Die	4/4/45°	4/4/45°	32/4/45°
Flow curve parameters			
ΔP_y(bar)	180	250	300
b (s/m^3)	82×10^6	45×10^6	82×10^6
n (−)	1/4	1/6	1/4
$\bar{\mu}$ (bar s/m^3)	17×10^6	20×10^6	25×10^6

The experimental observations in Fig. 4 show that during the unstable extrusion process there are extended periods during each oscillation cycle in which there is no material extruded from the die, followed by rapid events during which the velocity rapidly increases and the pressure drops. During the former part of the cycle, the fluid is unyielded (and ''sticks'' to the walls of the die) while the pressure climbs almost linearly in time indicating that the material is, in fact, weakly compressible. During the second part of the cycle, the material yields in a thin layer near the wall and rapidly flows out from the die in a sudden ''spurt,'' thus lowering the internal extruder pressure.

Georgiou and Crochet (1994a) (1994b) have recently discussed the use of a compressible Newtonian fluid model coupled with a nonlinear law for the slip velocity $u_s(\tau_w)$ at the wall as a mechanism for modeling spurt instabilities in polyethylene melts. Molenaars and Koopman (1994) adopt a different approach using both compressibility and a nonlinear rheological response and we follow a conceptually similar analysis. The key difference between the present work and previous experimental and theoretical studies of *spurtlike* instabilities is the existence of a finite yield stress in the material, which results in the *nonzero* yield pressure ΔP_y observed experimentally in the extruder (cf. Fig. 2). We do not have to invoke a nonlinear slip boundary condition to recreate the observed dynamics but instead use the experimentally measured steady flow curve for $\Delta P_f(Q_e)$ as the basis of the constitutive relationship for the chocolate extrudate.

At the start of an experiment, the extruder is filled with chocolate either as ground pieces or as individual ''buttons.'' The initial volume of the chocolate-filled reservoir depicted in Fig. 1 is denoted V_0 and the piston velocity is set to a constant value U_p so that the volume of the reservoir available to the chocolate decreases as

$$\frac{dV}{dt} = -A_\mathrm{p}U_\mathrm{p} = -Q_i\,, \tag{3.4}$$

where $A_\mathrm{p} = \pi D_\mathrm{p}^2/4$ is the area of the piston ($D_\mathrm{p} = 19.05$ mm) and Q_i denotes the rate at which the control mass decreases in volume (as specified by operator selection of the piston velocity U_p).

The extrudate velocity at the exit of the die is denoted U_e and the volumetric flow rate out of the extruder is $Q_e = A_eU_e$ where $R = D/2 = 2$ mm, and $A_e = \pi R^2 = 12.57\ \mathrm{mm}^2$. A material balance on the control mass of chocolate in the reservoir and die-land leads to

$$\frac{d}{dt}(\rho V) = -\rho Q_e\,, \tag{3.5}$$

where ρ is the density of the chocolate. The isothermal compressibility of the chocolate is denoted by

$$\chi = \frac{1}{\rho}\left(\frac{\partial \rho}{\partial P}\right)_T\,, \tag{3.6}$$

and has a value of $\chi \approx 10^{-9}\ \mathrm{m}^2/\mathrm{N}$ [Crook (1997)]. This value is assumed to correspond to that of the ''bulk'' chocolate present in the bed, encompassing that of the solid chocolate alone and also the possible presence of any bed voidage caused during compaction. Combining Eqs. (3.5) and (3.6) leads to

$$\frac{d(\Delta P)}{dt} = -\frac{(Q_e - Q_i)}{\chi V}. \tag{3.7}$$

Since the chocolate is initially in equilibrium at atmospheric pressure and is below its yield pressure, after an initial, extremely rapid period of void compaction surrounding the individual buttons the gauge pressure ΔP in the barrel begins to climb. While the chocolate remains unyielded, $Q_e = 0$ and Q_i is constant, therefore, at short times the pressure in the barrel climbs linearly with time as observed experimentally in Fig. 2. Eventually, the pressure in the extruder reaches the value ΔP_y and the material yields. A one-dimensional force balance on the accelerating cylindrical plug of chocolate results in

$$\rho \pi R^2 L_{\text{eff}} \frac{dU_e}{dt} = \pi R^2 [\Delta P - \Delta P_f(Q_e)], \tag{3.8}$$

where $\Delta P_f(Q_e)$ is the pressure obtained from the ''flow curve'' for the steady-state extrusion given by Eq. (3.3), and the exit velocity U_e can again be reexpressed in terms of the extrudate flow rate as $U_e = Q_e / \pi R^2$. The effective length of the yielded plug that accelerates is denoted L_{eff}. A simple force balance on the plug during steady-state motion results in

$$\Delta P_f \pi R^2 = 2\pi R L_{\text{eff}} \tau_w \Rightarrow \Delta P_f = \left(\frac{2L_{\text{eff}}}{R} \right) \tau_w, \tag{3.9}$$

and hence, it is apparent that the flow curve is a function of the aspect ratio of the die. For a given chocolate composition, the measured pressure difference should increase (approximately linearly) with the die die-land length L. A Bagley end correction plot [Dealy and Wissbrun (1990)] could be constructed from pressure-difference measurements with different L/R to evaluate the correction resulting from the entry flow region, however, we have not pursued such measurements in the present study. Numerical calculations of converging entry flows of isothermal Bingham plastics show that the length of this yielded plug region only extends slightly upstream into the mouth of the die [Papanastasiou (1987)].

Equations (3.7) and (3.8) are a coupled set of first-order differential equations, which are nonlinear due to the form of the steady extrusion flow curve $\Delta P_f = \Delta P_f(Q_e)$. The dynamics of the processes described by these equations can be understood more clearly by rewriting them in dimensionless form. We define a dimensionless pressure difference relative to the yield pressure by $p = \Delta P / \Delta P_y$ and a dimensionless flow rate by $q = Q_e / Q_i$. Substituting into Eq. (3.7) leads to

$$\frac{dp}{d\hat{t}} = 1 - q, \tag{3.10}$$

where $\hat{t} = t/t_c$ is the dimensionless time scale, and the characteristic time for compression of the material is $t_c = V\chi \Delta P_y / Q_i$.

Similarly, substituting the expressions for p, q, and t_c into Eq. (3.10) yields

$$\frac{dq}{d\hat{t}} = \frac{1}{W} [p - f(q)], \tag{3.11}$$

where $f(q) = \Delta P_f(Q_e)/\Delta P_y$. The dimensionless group W is defined by

$$W = \frac{\rho Q_i^2}{V\chi \Delta P_y^2} \frac{L_{\text{eff}}}{\pi R^2}, \tag{3.12}$$

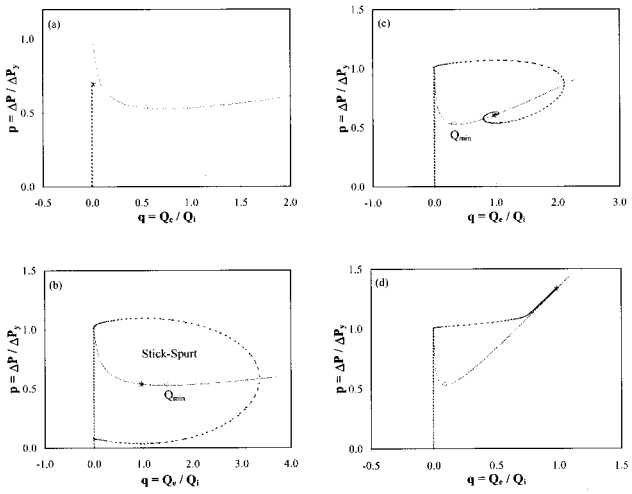

FIG. 5. Phase plane portraits for the dimensionless pressure difference $p(t)$ and flow rate $q(t)$ during the cold extrusion of chocolate with $W = 5\times10^{-2}$. The solid line indicates the steady flow curve $\Delta P_f(Q_e)/\Delta P_y$, the (*) denotes the externally imposed operating condition $q = Q_e/Q_i$, and the (○) denotes the minimum stable operating condition. (a) No flow, $\Delta P < \Delta P_y$, $Q_e = 0$; (b) $\Delta P < \Delta P_y$, $Q_i < Q_{\min}$, stick–spurt oscillations; (c) $\Delta P < \Delta P_y$, $Q_i > Q_{\min}$, pressure overshoot and damped oscillations to steady state; and (d) $\Delta P > \Delta P_y$, $Q_i \gg Q_{\min}$, monotonic pressure growth towards steady state.

and can be interpreted as either a ratio of the characteristic pressure fluctuations arising from inertial accelerations ($\sim \rho U_e^2$) to those resulting from compressibility ($\sim V\chi\Delta P_y^2$) or as a ratio of the characteristic time scale for inertial accelerations to the characteristic time t_c for isothermal compression of the chocolate sample to its yield pressure. As a result of the small volumetric flow rates and large extrusion yield pressures of the chocolate, typically, $W \ll 1$. Consequently, the equation set given by Eqs. (3.11) and (3.12) plus the nonmonotic constitutive relationship [Eq. (3.5)] form a stiff initial value problem, and these can be solved using standard numerical techniques such as the Gear algorithm [Press *et al.* (1986)].

The nonmonotonic viscoplastic response of the constitutive relationship for chocolate results in four distinct dynamical responses from this equation set. The temporal evolution of the system can be most clearly represented in the phase-plane diagrams of $\{p(t),q(t)\}$ shown in Fig. 5 for $W = 5\times10^{-2}$. If the chocolate is extruded at *constant pressure*, then there are two possible responses. For extrusion pressures below the yield pressure $\Delta P < \Delta P_y$, the chocolate is simply compressed to a new static configuration and there is no flow, as indicated in Fig. 5(a). At extrusion pressures above the yield point ($\Delta P > \Delta P_y$), the chocolate is initially compressed, then yields and the fluid rapidly accelerates to a new steady and stable exit velocity corresponding to $\Delta P_f = \Delta P_f(Q_e)$ given by Eq. (3.3), as shown in Fig. 5(d).

Alternatively, if the extruder is operated at constant *crosshead speed*, as is the case for the Davenport rheometer employed in the present work, then the dynamics are more complex as a result of the multiple solutions for the steady flow pressure ΔP_f below ΔP_y. For $Q_i > Q_{\min}$ and $\Delta P < \Delta P_y$, the response is shown in Fig. 5(c). Again, the pressure increases to the yield value, the fluid accelerates, and overshoots its steady extrusion velocity. The fluid pressure and extrusion rate then undergo a series of underdamped oscillations of decreasing amplitude about the final stable fixed point on the flow curve. The relaxation rate of these oscillations and the approach to steady state depend on

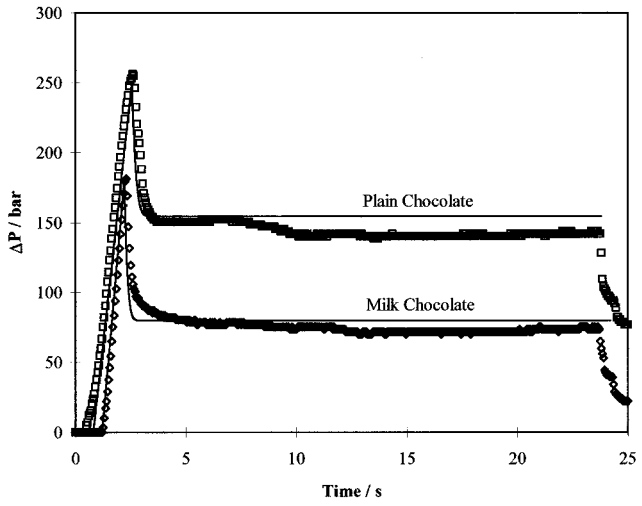

FIG. 6. Model predictions of the relaxation–oscillation model for initial pressure transient during steady cold extrusion of chocolate. (□) = plain chocolate, 20 °C, 4/4/45°; (◇) = milk chocolate, 20 °C, 4/4/45°. The solid lines indicate the model predictions for the parameters in Table III plus $Q_i = 1.608\times10^{-6}$ m^3/s corresponding to $t_c = 1.77$ s (plain chocolate), 1.02 s (milk chocolate), and $W = 7.70\times10^{-6}$ (plain chocolate), 1.86×10^{-6} (milk chocolate).

the magnitude of the dimensionless group, W. Finally, for $Q_i < Q_{\min}$ and $\Delta P < \Delta$Py the response is shown in Fig. 5(b). Here, the chocolate is compressed, yields, and accelerates as before, however, the oscillations do not decay in time and the pressure and extrudate volume flow rate follow a *limit cycle* about the periodic attractor located at $\Delta P_f = \Delta P_f(Q_e)$. The chocolate initially yields and rapidly accelerates or ''spurts,'' then subsequently decelerates as the pressure in the reservoir falls, until the velocity drops to zero again and the fluid sticks to the die walls. The pressure then climbs again as the crosshead compresses the static unyielded chocolate until the yield pressure is reached and the cycle repeats. The period of oscillations depends on the time scale t_c and the value of W. We refer to this limit cycle as a *stick–spurt* response to distinguish it from typical ''constitutive instabilities'' and spurt phenomena associated with slip boundary conditions [Larson (1992)]. The existence of a finite yield stress in the material eliminates the stable lower branch of the flow curve in the stick–slip analysis and there are extended periods of time during which no material exits the extruder at all ($q = 0$).

In Fig. 6, the predictions of this relaxation oscillation model are compared with the transient pressure data for milk and plain chocolate previously presented in Fig. 2. Substituting the appropriate numerical values for Q_i and χ plus the geometric dimensions of the extruder yields a characteristic time of $t_c = 1.77$ s for the plain chocolate to reach the yield pressure, and the dimensionless parameter value of $W = 7.7\times10^{-6}$. The pressure initially climbs linearly in time to the yield pressure then rapidly drops and monotonically approaches a steady state with $Q_e = Q_i > Q_{\min}$ and $\Delta P_{\min} < \Delta P_f < \Delta P_y$. A sequence of underdamped or relaxing oscillations is not observed in this case because of the very small value of W. For milk chocolate, the yield pressure is lower, hence, the time scale is computed to be only $t_c = 1.02$ s, and the extrusion rate Q_i corresponds to $W = 1.86\times10^{-6}$. In both cases, the model provides a good description of the pressure overshoot and initial approach to steady state. The gradual drop in the pressure at longer

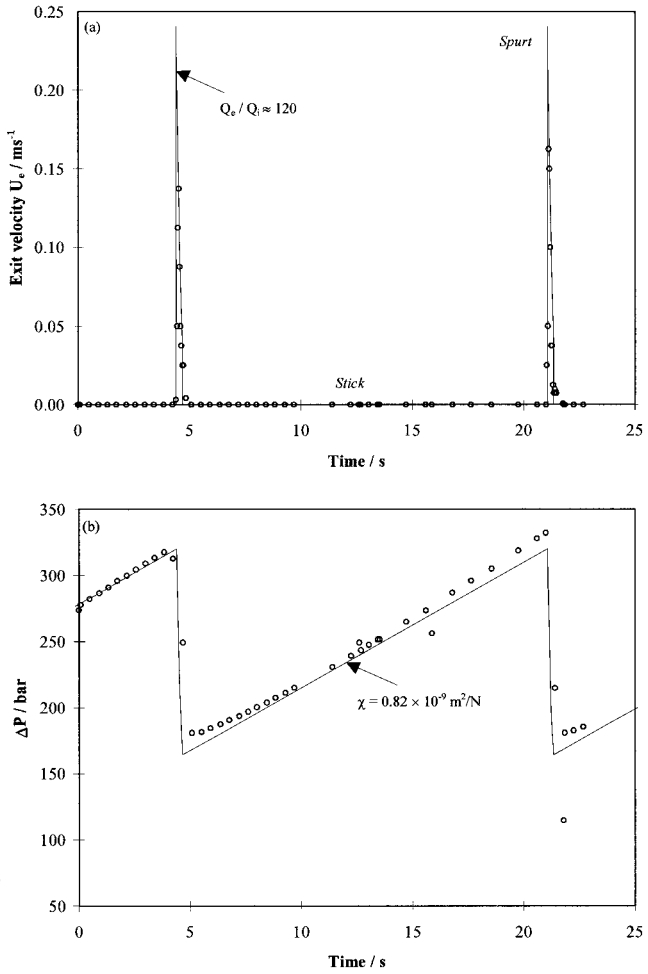

FIG. 7. Stick–spurt oscillations in the cold extrusion of milk chocolate at 16 °C through a 32/4/45° die. The flow rate is $Q_i = 2.5\times10^{-8}$ m^3/s and the reservoir volume corresponds to $t_c = 33.70$ s and $W = 9.4 \times10^{-10}$. The compressibility of chocolate is ascertained from the rate of increase in extrusion pressure to be $\chi = 0.82\times10^{-9}$ m^2/N.

times observed experimentally is not captured by the model and possibly arises from the gradual decrease in the volume of the chocolate in the barrel or from a slow local dissipative heating and associated softening of the chocolate in the barrel.

At lower piston velocities, the imposed or ''desired'' extrudate volume flow rate Q_i drops below the minimum stable operating condition $Q_i < Q_{\min}$ and stick–spurt oscillations develop. The measured oscillations in the pressure $\Delta P(t)$ and extrudate velocity $U_e = Q_e(t)/A_e$ are shown in Fig. 7, at a reservoir volume corresponding to $t_c = 33.7$ s and $W = 9.4\times10^{-10}$. The imposed flow rate was 2.5×10^{-8} m^3/s. The only uncertainty in any numerical quantity is the value of χ for the chocolate, and this parameter primarily affects the slope of the pressure increase with time during the ''stick'' or compression part of the cycle. The fitted value obtained from the simulation shown in Fig. 7 is $\chi = 0.82\times10^{-9}$ m^2/N, which is physically realistic. As the piston velocity is increased, the characteristic time t_c decreases and the frequency of stick–spurt

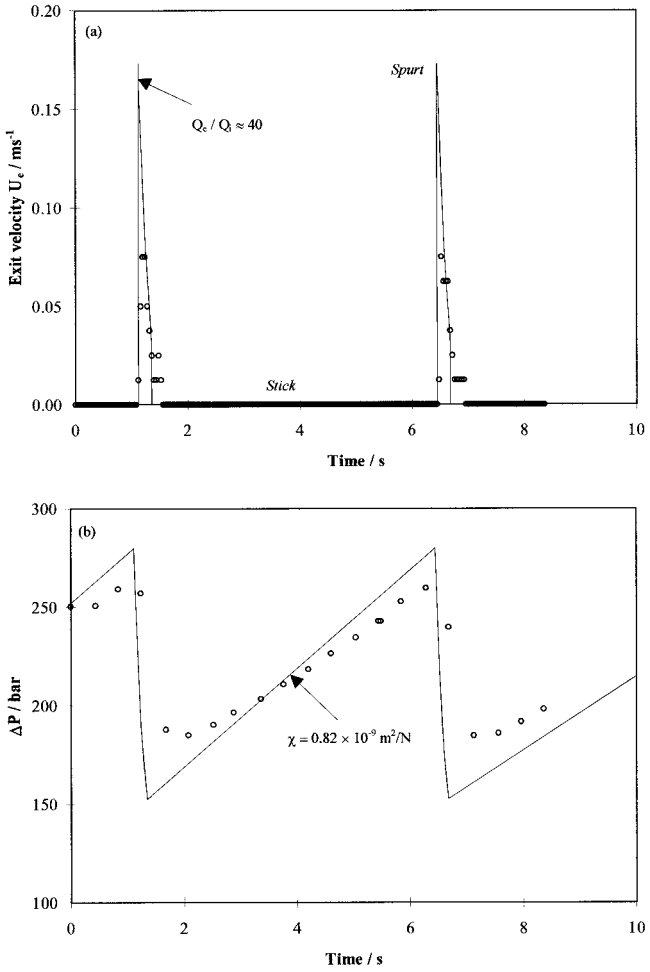

FIG. 8. Stick–spurt oscillations in the cold extrusion of milk chocolate at 16 °C through a 32/4/45° die. The flow rate is $Q_i = 5.0\times10^{-8}$ m^3/s and the reservoir volume corresponds to $t_c = 16.85$ s and $W = 3.0 \times10^{-9}$.

oscillations increases. In Fig. 8, the fluctuations in $\Delta P(t)$ and $Q_e(t)$ at a constant crosshead speed corresponding to an imposed flow rate of $Q_i = 5\times10^{-8}$ m^3/s are shown together with the predictions of the stick–spurt equations, and the same value of χ obtained above. The period of oscillations is predicted to decrease in good agreement with the experimental observations, and the pressure fluctuations maintain their characteristic sawtooth form. In both Figs. 7 and 8, the numerically predicted magnitudes of the maximum spurt amplitude $(U_e/U_i)_{\max}$ are somewhat higher than those observed experimentally. This is because we compute the experimental values of the extrudate velocity U_e by observing the displacement of the extruded plug of chocolate on consecutive video frames with a temporal resolution of 1/25$^{\text{th}}$ s, and such finite difference estimates cannot accurately resolve the most rapid spurt events.

It is clear from the results in Figs. 7 and 8 that the stick–spurt analysis is capable of capturing the dynamics of the oscillations in pressure and extrudate velocity observed

experimentally as well as the crossover to stable extrusion at higher piston speeds corresponding to $Q_i = Q_e > Q_{\min}$. The characteristic time scale t_c for the pressure transients observed upon the inception of stable extrusion as well as in the unsteady periodic ''stick–spurt'' oscillations is found to be a function of the material (the yield stress), the geometry (i.e., the volume of the reservoir), and the imposed crosshead speed U_p, and can, thus, be controlled by a judicious choice of operating conditions. More detailed consideration of the radial velocity profile obtained in the accelerating fluid plug exiting the die may also be able to explain the nonuniform extrudate shape, however, in order to extend the analysis, it is necessary to determine the location of the yield surface near the wall of the capillary and the radial extent of the plug–flow region in the core of the die-land. Such a two-dimensional analysis must be pursued numerically.

IV. THE ''OVAICI NECKLACE'' INSTABILITY

In the course of carrying out a series of experiments to establish the effect of initial feed particle size on cold extrusion, an experiment was carried out where molten chocolate was poured into the reservoir, cooled in the rheometer, and then cold extruded as a solid mass. This chocolate had not, therefore, been tempered in the usual way and consequently gave rise to an initially surprising extrusion profile when subsequently cold extruded. For the large amplitude free-surface fluctuations and the resulting beads-on-a-string structure, we have named the form of the extrusion the ''Ovaici necklace.''

A. Experimental observation

In order to observe the Ovaici necklace effect a very specific preprocessing thermal protocol must be followed. Plain chocolate was initially heated to 70 °C and maintained at that temperature for a period of 90 min. The fully molten chocolate was then shaken and ''tapped'' until no more air bubbles evolved, this degassed chocolate was then poured into the barrel of the Davenport rheometer, which was held at a temperature of 19 °C. The temperature of the molten chocolate just prior to being poured in the rheometer was measured to be approximately 58 °C. For the experiments described in this section, a die of 4 mm diam, 4 mm die-land length, and an entry angle of 45 ° was used. The chocolate was allowed to crystallize in the barrel of the rheometer for 3 h at 19 °C. After that time, the barrel temperature was raised to 22 °C and the chocolate left for a further 21 h at that temperature.

The cold extrusion experiment was carried out in the same way as in the previous sections, but starting with the barrel crystallized chocolate rather than tempered chocolate pieces. Figure 9(a) shows the observed pressure trace as a function of time. After yield, a stable extrusion is observed for a limited period of time. This is then followed by a period when the extrusion pressure rises and during this period Ovaici necklaces are formed. As the piston advances further down the barrel, necklace formation ceases and the extrusion pressure drops to its original steady value. Figure 9(b) shows a close up of the pressure trace as a function of time within the necklace formation zone. The extrusion pressure is slightly higher than that for Fig. 9(a) as these are two separate experiments, and is believed to be due to uncontrollable variations in the chocolate composition, or small changes in extrusion conditions such as temperature or flow rate. From Fig. 9(b) it can be observed that the extrusion pressure is not constant over the necklace formation zone, but it asymptotically rises to a characteristic maximum or ''break'' pressure as the length of the extruded bead increases, and then suddenly falls to a characteristic lower pressure as the bead breaks and is advected away from the die exit. The pressure fluctuation is then repeated as another bead forms.

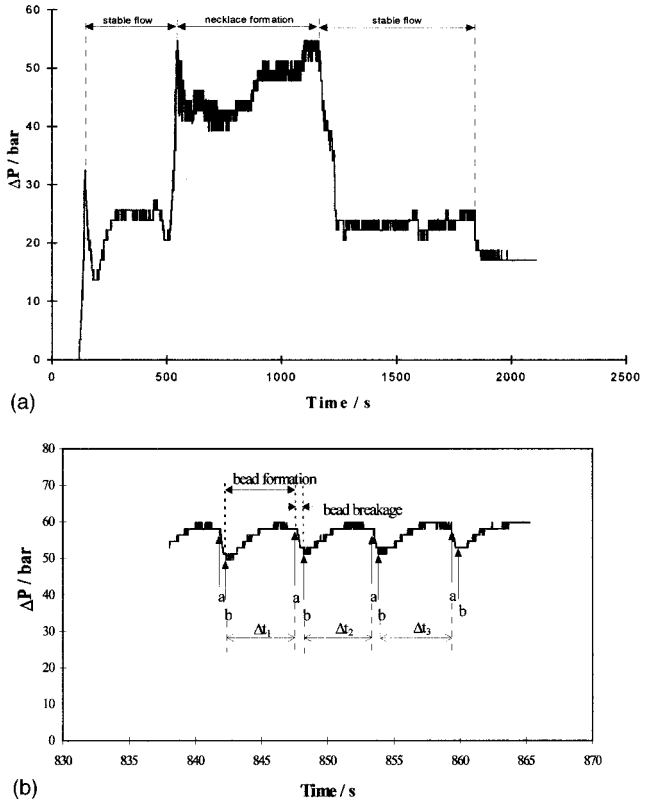

FIG. 9. (a) Pressure difference as a function of time during a typical ''Ovaici'' necklace flow instability experiment using plain chocolate. Q_e (using the Davenport rheometer) = 30.78 mm^3/s, die = 4/4/45°, T = 22 °C. Data logged at a rate of 4 Hz. (b) Pressure difference as a function of time during the Ovaici necklace flow instability zone. Q_e (using the Davenport rheometer) = 30.78 mm^3/s, die = 4/4/45°, T = 22 °C. Data logged at a rate of 50 Hz. a = Onset of bead breakage, b = Total breakage of bead and start of subsequent bead formation, Δt_{a-b} = breakage time = 0.4 s (approx.), $\Delta t = (\Delta t_1 + \Delta t_2 + \Delta t_3)/3$ = 5.7 s (approximate) for L_B = 9 mm (approximate).

The time evolution of the corresponding extrusion is shown in Fig. 10. The initial extrudate is continuous, followed by a period of unstable flow where the continuous extrudate becomes grossly distorted, followed by a period of necklace formation, and finally a return to continuous extrusion. During a single extrusion experiment, necklace beads of varying length and varying distance between adjacent beads were obtained. Table IV summarizes this range for a specific case. The diameter of the bead (D) was always the same as the die exit diameter, however, the diameter of the thin connecting thread (d), the length of bead (L_B), and the length of the thread between two adjacent beads (L_T) were found to be strongly interrelated; a small diameter of thread resulted in a larger length of bead and a larger distance between adjacent beads. A larger diameter of thread had the opposite effect. The flow rate was also found to have a significant effect on the length of the thread between adjacent beads, but not on the size of the bead, as shown in Table V. In general, a slower flow rate resulted in larger distances between adjacent beads, and conversely, a higher flow rate lead to shorter distances.

Representative photographs of the Ovaici necklaces are shown in Figs. 11 and 12. The necklace has the form of a continuous 2 mm diam chocolate core onto which 4 mm diam

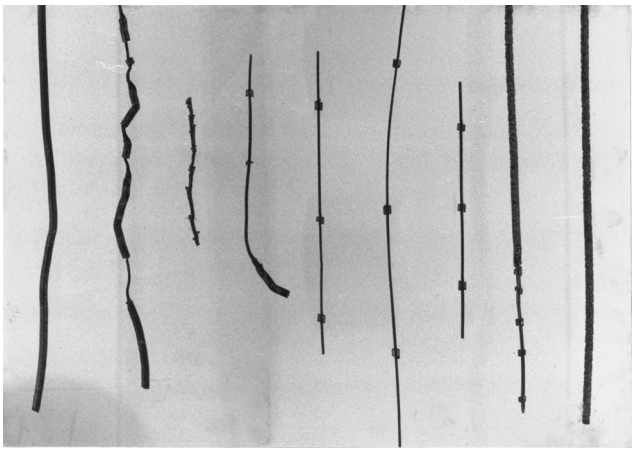

FIG. 10. Photograph of extrusion profile evolution, correlating with extrusion pressure vs time diagram in Fig. 9(a). Start of extrusion, bottom, left-hand side (LHS) of photograph. Termination of extrusion, top right-hand side (RHS).

annular chocolate beads appear at regular intervals along the core. The overall appearance of the extrudate is similar to that of a necklace, and the initial flexibility of the chocolate means that the extrudate can be bent to further enhance the appearance of the necklace, as shown in Fig. 11. The higher magnification photograph shown in Fig. 12 suggests that the necklace is formed from two components, an inner core and the periodically spaced outer annular beads. The faces of the beads are perpendicular to the extrusion direction and the sharp interfaces strongly suggest that they have been created by some form of fracture mechanism.

The suggestion that the extrusion is formed from two distinct chocolate components is supported by two further pieces of experimental evidence. Figure 13 shows a series of photographs of extruded sections of chocolate that had been removed from the barrel. Each sample constitutes a separate experiment, which had been terminated at different times. The sample was removed from the barrel, sectioned in half, and then left for a period of a week. During this time the inner core of chocolate was seen to ''bloom,'' indicating decomposition of a metastable chocolate phase [Beckett (1994)] leaving a sharp contrast with a nonblooming component near the walls of the barrel. The conditions leading to formation of the Ovaici necklaces corresponds to coextrusion of these two chocolate components. The second piece of evidence supporting two component coextrusion is found from postmortem studies of the extruded necklace itself. Figure 14 shows differential scanning calorimetry (DSC) traces of a necklace sample. Figure 14 shows

TABLE IV. Range of thread thickness, bead length, and bead spacing observed during an Ovaici necklace experiment for Q_e (using the Davenport rheometer) $= 30.78\ \text{mm}^3/\text{s}$, Die = 4/4/45°. $T = 22$ °C. The parameters D, d, L_B, and L_T are indicated schematically in Fig. 15.

	Maximum value (mm)	Minimum value (mm)	Median value (mm)
Diameter of bead, D	4	4	4
Diameter of thread, d	3	1	1.5
Length of bead, L_B	9	2	5
Length between adjacent beads, L_T	110	10	60

TABLE V. Range of thread thickness, bead length, and bead spacing observed during an Ovaici necklace experiment for Q_e (using the Davenport rheometer) = (30.78/2) mm^3/s, die = 4/4/45°, T = 22 °C.

	Maximum value (mm)	Minimum value (mm)	Median value (mm)
Diameter of bead, D	4	4	4
Diameter of thread, d	2	1	1.5
Length of bead, L_B	9	2	5.5
Length between adjacent beads, L_T	225	10	120

three traces. The trace for a whole necklace bead shows a curve with two distinct melting peaks. By contrast, DSC analysis of the outer annular region alone shows only one peak corresponding to the higher melting point value, while the core also has a single peak corresponding to the lower melting value of the whole necklace bead. From this data, we conclude that the necklace is formed from a coextrusion of two distinct chocolate phases, the higher melting point of the annular bead suggesting that it is of a more stable crystal form and probably harder than the inner component that forms the thread of the necklace. Figure 15 shows the schematic diagram of a necklace, showing one chocolate component passing through the other, and the location of the two chocolate components in the extrusion rheometer prior to extrusion.

B. Mechanism and modeling of the Ovaici necklace

The experimental observations indicate that the necklace beads have a core–annular structure corresponding to two of the polymorphic crystalline forms of chocolate [Beckett (1994)], most likely ''form IV'' and ''form V.'' The thermally more stable chocolate ($T_m \approx 32$ °C) is also to be expected to be mechanically stronger with a higher yield stress than the ''form IV.'' Furthermore, direct observation of the extrudate shows that during the period of necklace formation the inner core is extruded at a constant rate. The outer bead also extrudes continuously, but at a slower rate than the core. After a certain length of time, the outer annulus of chocolate fractures at the exit face of the die and the annular bead that has been formed is advected away from the face of the die with a

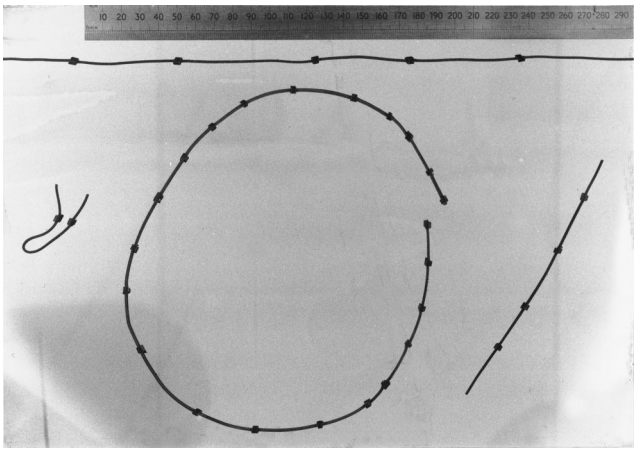

FIG. 11. Photograph of Ovaici necklace showing four examples of necklace formation including one necklace with curved contour demonstrating the residual flexibility following cold extrusion.

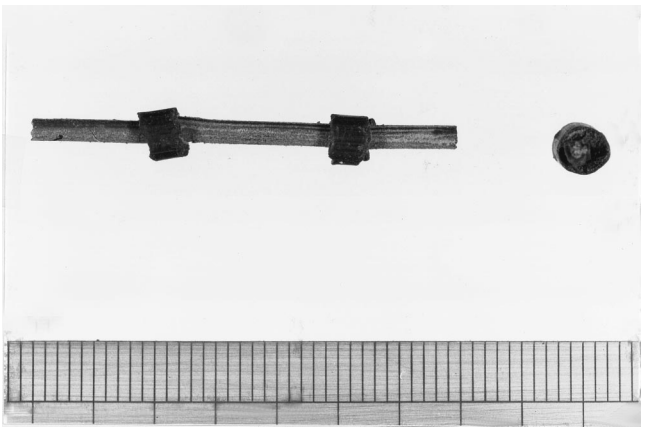

FIG. 12. High magnification photograph of Ovaici necklace (1 digit on ruler = 1 mm).

velocity equal to that of the inner core. This leaves the outer annulus to continue to extrude at the slower rate, thereby allowing the mechanism to repeat successively, forming periodic beads along the core. The effect is shown schematically in Fig. 16.

The data in Tables IV and V show that the bead diameter is always given by the die diameter (D) but that the spacing between beads (L_T) increases sharply as the flow rate is decreased. The overall features of this ''Ovaici necklace'' instability can be captured by assuming that the two chocolate phases are coextruded in a core–annular configuration. The pressure oscillations shown in Fig. 9(b) are small in amplitude ($\chi \Delta P_v / \Delta P_f \approx 1.49 \times 10^{-10}$ m^2/N) and, in contrast to Sec. III, compressibility effects are not important here. Furthermore, since the temperature is higher (22 °C) and the material has been thermally pretreated, the steady flow curves $\Delta P_f(Q_e)$ for the chocolate are not double valued, and consequently, the two phases can be treated as two immiscible Bingham plastics, which we label A and B and which are arranged in an axisymmetric

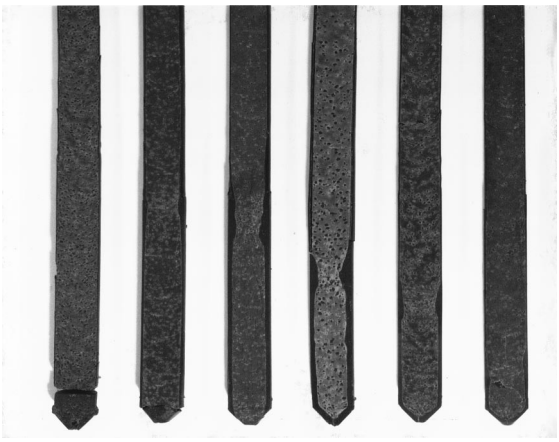

FIG. 13. Photographs of billets showing cut sections of billets remaining in the barrel of the Davenport rheometer. LHS, no extrusion. RHS, near end of necklace formation. All photographs show a metastable phase (bloomed) of core chocolate with stable (darker) chocolate near the barrel wall.

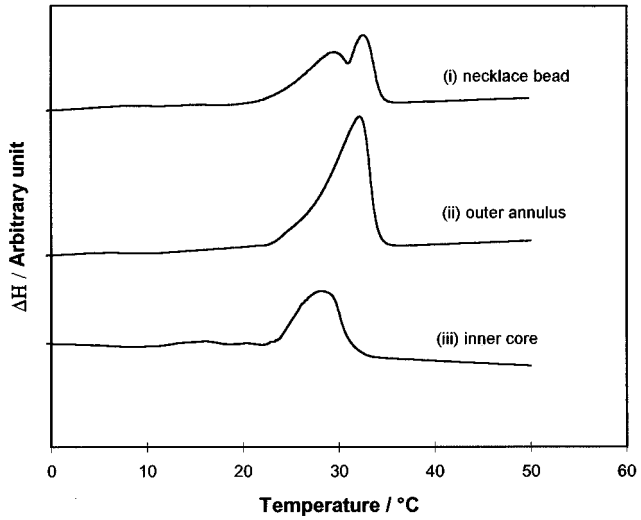

FIG. 14. Differential scanning calorimetry (DSC) of a typical necklace: (i) thermogram of a necklace bead, (ii) thermogram of outer annulus of necklace bead, and (iii) thermogram of inner core of necklace bead. Average sample weight = 10 mg, and heating rate = 10 °C/min.

core–annular configuration as shown schematically in Fig. 17. The generalized Bingham-plastic constitutive equation of each phase can be simplified for unidirectional shear flow to

$$\tau^{\mathrm{A}} = \tau_y^{\mathrm{A}} + \mu^{\mathrm{A}}\dot{\gamma}, \tag{4.1}$$

$$\tau^{\mathrm{B}} = \tau_y^{\mathrm{B}} + \mu^{\mathrm{B}}\dot{\gamma}, \tag{4.2}$$

where τ_y^{A}, τ_y^{B}, μ^{A}, and μ^{B} are the respective yield stress and viscosities for each material, and τ is the shear stress, and $\dot{\gamma} = |dv_z/dr|$ is the velocity gradient in the die. We further assume that the boundary between the A and B components occurs at a specified radial position given by $X = r_i/R$, where $R(= D/2)$ is the inner radius of the die and r_i is the radial location of the interface. There are at least nine possible kinematic configurations of the resulting velocity field depending on the relative values of τ_y^{A}, τ_y^{B} and the imposed stress $\tau = (\Delta P_f/L)(r/2)$. If τ_y^{B} is greater than τ_y^{A}, it is shown in the appendix (Sec. 1) that regions within each phase of A and B can move in plug flow with velocities given by

$$v_{\mathrm{plug}}^{\mathrm{B}} = \frac{R\tau_w}{2\mu^{\mathrm{B}}}(1-\mathrm{Bi}^{\mathrm{B}})^2, \tag{4.3}$$

$$v_{\mathrm{plug}}^{\mathrm{A}} = v_{\mathrm{plug}}^{\mathrm{B}} + \frac{R\tau_w}{2\mu^{\mathrm{A}}}(X-\mathrm{Bi}^{\mathrm{A}})^2, \tag{4.4}$$

where τ_w is the wall shear stress and Bi is the Bingham number for each component, defined as

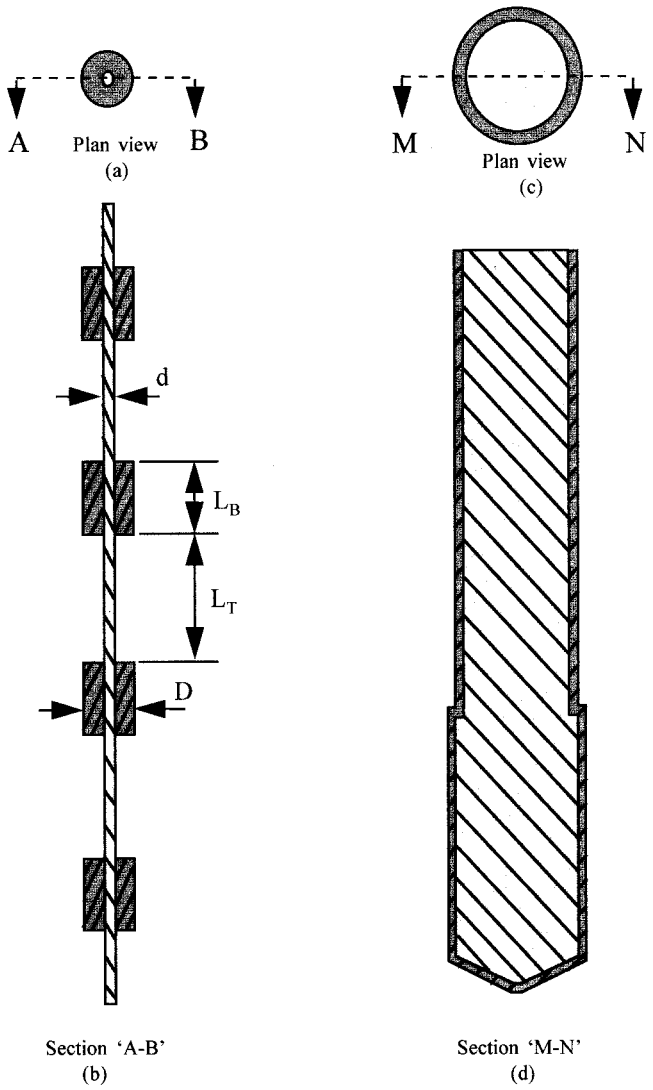

FIG. 15. Schematic diagram of ''Ovaici'' necklace and location of the two-component phases of chocolate in the extrusion rheometer prior to extrusion: (a) plan view of a typical necklace showing two-component chocolate, (b) cross-sectional view of necklace indicating that the inner, continuous component passes through the outer discrete phases, (c) plan view of position of two-component chocolate in the Davenport rheometer prior to extrusion, and (d) cross-sectional view of position of two-component chocolate in the Davenport rheometer prior to extrusion. D = diameter of bead, L_B = length of bead, d = diameter of thread (inner core), L_T = length of thread between two adjacent beads.

$$\mathrm{Bi}^A = \frac{\tau_y^A}{\tau_w}, \quad \mathrm{Bi}^B = \frac{\tau_y^B}{\tau_w}.$$

These plug flow regions are connected by narrow ''slip layers'' within which the material has yielded. A simple force balance in the die gives $\tau_w = (\Delta P_f R/2L)$. We now have two equations giving the plug flow velocities of A and B components where

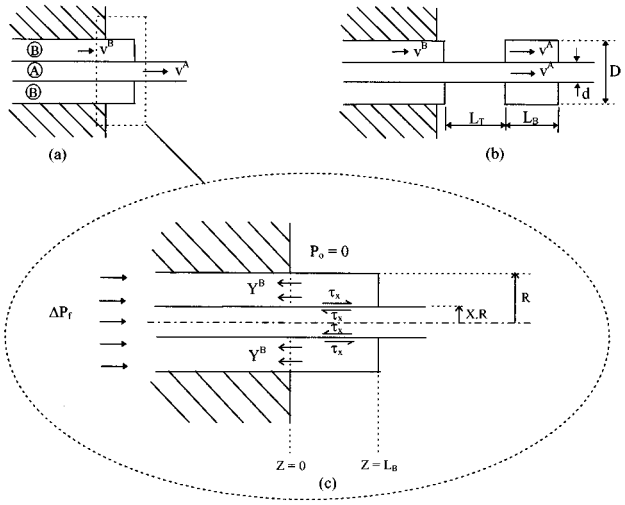

FIG. 16. Schematic diagram showing the formation of a necklace bead. The plug velocity of the core is greater than that of the outer annulus, $v^A > v^B$, where v^A, v^B = characteristic velocity of materials A and B, respectively. After a period of time, the outer annulus of chocolate fractures at the exit face of the die and the annuluar bead that has been formed is advected away from the face of the die with a velocity equal to that of the inner core. (a) necklace bead being formed at the exit face of the capillary section of the die, (b) bead formed and being advected away from the die face, and (c) free-body diagram showing forces acting on phases A and B.

$v^A_{plug} > v^B_{plug}$. The predicted shear stress and velocity profile region is shown schematically in Fig. 18, and the dimensionless location of the yield surfaces is given by $\xi_1 = \mathrm{Bi}^A$ and $\xi_2 = \mathrm{Bi}^B$. The flow divides into four regions. Two regions of plug flow in which the stress is below the yield stress of that phase and two narrow ''boundary layers'' of viscous flow. By integrating across the velocity profile it is possible to obtain a further equation for the total volumetric flow, as shown in the appendix (Sec. 3).

In Figs. 16(a) and 16(b) we schematically show a bead as it is being formed. We envisage continuity of velocity and shear stress at the interface (i.e.,

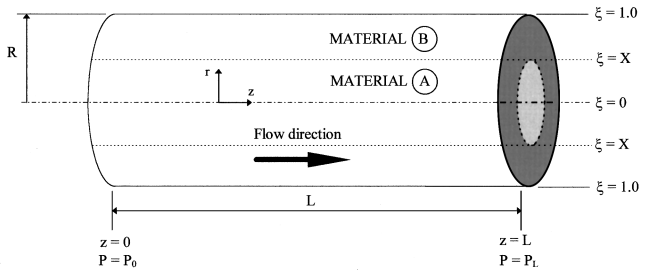

FIG. 17. Schematic diagram of a cylindrical die-land with materials A (soft) and B (hard) arranged in the core–annular configuration. Material B is next to the tube wall and material A in the core. ξ = dimensionless variable = r/R, where R = inner radius of cylindrical tube and r = an internal radial dimension. The radial location of the boundary between materials A and B is denoted $X = r_i/R$, where r_i = radial position of the interface. z = axial position along the tube, P = pressure, and for a rectilinear flow the pressure drop is related to the wall shear stress by $\Delta P/L = (P_0 - P_L)/L = 2\tau_w/R$.

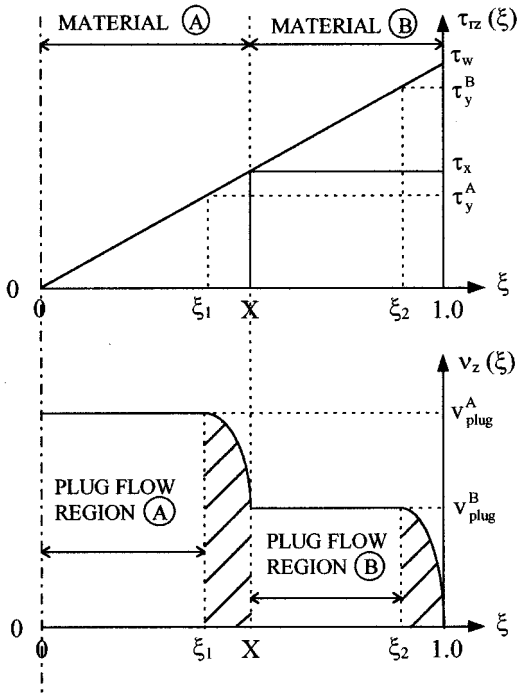

FIG. 18. Shear stress and velocity profile during the coaxial annular flow of the two chocolate components A and B. The flow is divided into four regions; two regions of plug flow and two narrow ''boundary layers'' of viscous flow: τ_w = shear stress at cylindrical tube wall; τ_x = shear stress at the interface between materials A and B; τ_y^A, τ_y^B = yield shear stress of materials A and B, respectively; v_{plug}^A, v_{plug}^B = plug velocities of materials A and B, respectively. The diagonal lines indicate position of the sheared region where $|\tau_{rz}(\xi)| > \tau_y^A$ or τ_y^B.

$|\tau_{rz}^A| = |\tau_{rz}^B| = \tau_x$) between the core and bead, plus zero slip between the bead and capillary wall. The velocity of the core is greater than that of the bead, and consequently, a shear stress will exist at the core/bead interface. A simple force balance, as shown Fig. 16(c), shows that material A in the region $0 < Z < L_B$ is in compression from the internal extrusion pressure ΔP_f and the shear stress τ_x acting on the circumference of the core region. By contrast, the outer free surface of the extruded annulus B is stress free in the region $0 < Z < L_B$, and the shear stress τ_x at the interface can only be balanced by a tensile stress Y^B in the annular region material immediately adjacent to the die exit. Chocolate, like many granular composite materials (e.g., concrete), is strong in compression but intrinsically weak in tension, and as the length of the extruded bead increases, the core–bead area over which the shear stress acts also increases. It can be readily envisaged that a situation is reached when the force at the core/bead interface reaches the fracture strength of the outer bead. At this point, shown in Fig. 16(b), the bead will detach from the outer annular extrudate, and subsequently, advect away from the die with the inner core velocity. The appropriate force balance can be obtained by reference to Fig. 16(c). At the instant of fracture and formation of a new bead, the shear stress acting on the perimeter of the core region (due to the relative motion of A and B at the interface X) is balanced by the tensile strength of the annular B-component material at the exit of the die. This yields

$$2XL_{\mathrm{B}}\tau_x = Y^{\mathrm{B}}R(1-X^2), \tag{4.5}$$

where L_{B} is the length of the necklace bead and Y^{B} the tensile yield stress of component B. The bead length L_{B} can be expressed as

$$L_{\mathrm{B}} = \frac{R}{2}\left(\frac{Y^{\mathrm{B}}}{\tau_w}\right)\left(\frac{1}{X^2}-1\right). \tag{4.6}$$

Using our knowledge of the time for formation of a necklace bead, $\Delta t = L_{\mathrm{B}}/v^{\mathrm{B}}_{\mathrm{plug}}$, and the equation for $v^{\mathrm{A}}_{\mathrm{plug}}$, it is then possible to determine the length L_{T} shown in Fig. 16(b). The length of thread between two adjacent beads is defined by $L_{\mathrm{T}} = \Delta t(v^{\mathrm{A}}_{\mathrm{plug}} - v^{\mathrm{B}}_{\mathrm{plug}})$, and is given by

$$L_{\mathrm{T}} = \frac{R}{2}\left(\frac{Y^{\mathrm{B}}}{\tau_w}\right)\left(\frac{1}{X^2}-1\right)\left(\frac{\mu^{\mathrm{B}}}{\mu^{\mathrm{A}}}\right)\left(\frac{X-\mathrm{Bi}^{\mathrm{A}}}{1-\mathrm{Bi}^{\mathrm{B}}}\right)^2. \tag{4.7}$$

Equations (4.6) and (4.7) give the two characteristic length scales of the Ovaici necklace expressed in terms of geometrical length scales R and X, rheological parameters τ_y^{A}, τ_y^{B}, μ^{A}, and μ^{B}, the tensile yield stress of the B component, Y^{B}, and the wall shear stress τ_w. It is now possible to fit the predictions of the model to a number of experimental examples for necklace formation; however, there are a large number of material parameters with magnitudes that cannot easily be obtained by independent measurement on each phase A, B. Equation (4.7), however, only requires knowledge of the ratios of the material parameters for the two phases. We have simplified the problem assuming that the tensile yield stress of component B is linearly related to the Bingham yield stress by

$$Y^{\mathrm{B}} = \alpha\tau_y^{\mathrm{B}}. \tag{4.8}$$

For a simple isotropic elastic material, $\alpha = \sqrt{3}$ corresponds to a Von Mises yield criterion and $\alpha = 2$ corresponds to the Tresca criterion. However, for a complex, partially crystalline material we can only expect $\alpha \geqslant 1$. From extrusion pressure measurements of the A and B component chocolate separately, we believe the yield stress of each component to be given approximately by

$$\frac{\tau_y^{\mathrm{B}}}{\tau_y^{\mathrm{A}}} \approx 3. \tag{4.9}$$

In addition, we make the semiarbitrary assumption that the viscosity ratios are given by the same factor, hence,

$$\frac{\mu^{\mathrm{B}}}{\mu^{\mathrm{A}}} = 3. \tag{4.10}$$

We now fit the data to one observed situation, namely $R = 2$ mm, $r_i = 0.96$ mm, $X = 0.48$, $L_{\mathrm{B}} = 3$ mm, $L_T = 11.2$ mm. These values correspond to the necklace shown in Fig. 12. The flowrate was 30.78 mm^3/s (using the Davenport rheometer), the die geometry was 4/4/45°, and the extrusion temperature was 22 °C. By using Eq. (4.6), and choosing $\alpha = 1.1$, it is possible to predict that $\mathrm{Bi}^{\mathrm{B}} = 0.8165$. Using this value and Eq. (4.7) yields a value of $\mathrm{Bi}^{\mathrm{A}} = 0.2753$, which in turn gives a yielded boundary layer thickness of $\delta\mathrm{B} = (1-\xi_2) = (1-\mathrm{Bi}^{\mathrm{B}}) = 0.1835$ and $\delta\mathrm{A} = (X-\xi_1) = (X-\mathrm{Bi}^{\mathrm{A}}) = 0.2047$. The self-consistency of this data can be tested with the mass balance equation, and we find the values given above are in good agreement to -1.3%. Figure 19

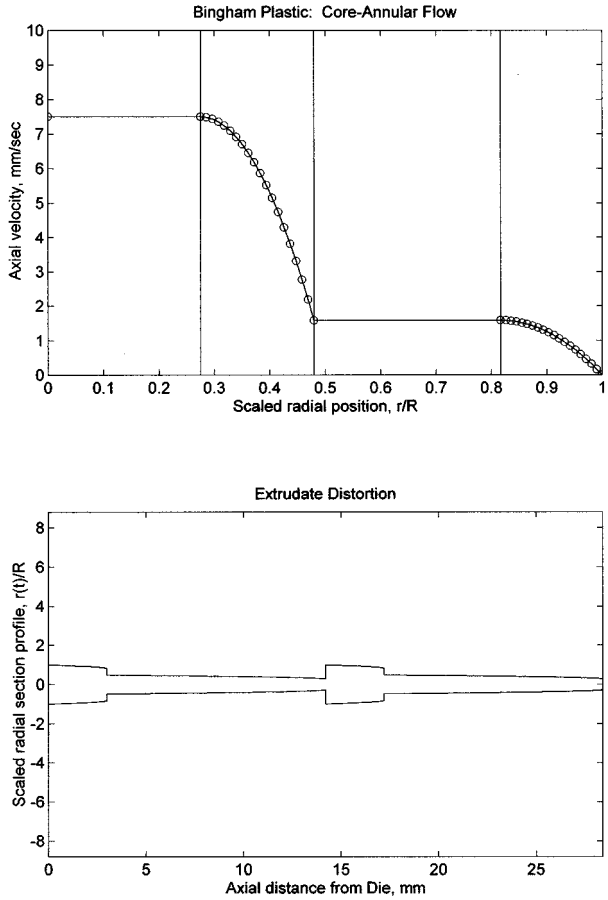

FIG. 19. Model simulation of the Ovaici necklace shown in Fig. 12; radial velocity profile and radial section profile. $R = 2$ mm, $X = 0.48$, $\alpha = 1.1$, $\mathrm{Bi}^{\mathrm{A}} = 0.2753$, $\mathrm{Bi}^{\mathrm{B}} = 0.8165$, $(\mu^{\mathrm{B}}/\mu^{\mathrm{A}}) = 3$, $\mu^{\mathrm{A}} = 0.00708\tau_w$ bar s, $\mu^{\mathrm{B}} = 0.02125\tau_w$ bar s. Thickness of yield regions $\delta\mathrm{B} = 0.1835$ and $\delta\mathrm{A} = 0.2047$.

shows the resulting model simulation of the velocity profile and predicted extrudate profile. The radial section profile matches the radial section profile of the necklace. It also predicts the slight taper in the length of the thread between the two beads and also along the length of each bead (cf. Fig. 12). From the radial velocity profile, the model predicts that the inner core material travels approximately five times faster than the material at the outer annulus, which is in good agreement with visual observations. The more rapidly extruding central core convects the beads away from the die exit face (at $Z = 0$), and forms the interlinking necklace.

Up to this point, we have shown that the model is capable of predicting the Ovaici necklace providing certain assumptions are made and parameter fitting carried out. We have also attempted to use the model in a truly predictive mode by assuming that the location of the yield surfaces and δB and δA depend on flow rate only as expected for a Bingham plastic. Table VI compares the experimental data with the model prediction for three other, quite widely different, observed situations. The flow rate in all three cases is the same as that in Fig. 12, only the ratio of the diameter of the inner core to that of the

TABLE VI. Observed data and model prediction of three different Ovaici necklaces. % error is defined according to $[(M-E)/E]\times 100$. Q (using the Davenport rheometer) $= 30.78\ \text{mm}^3/\text{s}$, die = 4/4/45°, $T = 22\ °\text{C}$. Case III corresponds to the median value data reported in Table IV.

	Case (I)			Case (II)			Case (III)		
	L_B (mm)	L_T (mm)	Q (mm^3/s)	L_B (mm)	L_T (mm)	Q (mm^3/s)	L_B (mm)	L_T (mm)	Q (mm^3/s)
Experimental data (E)	4.00	43.00	30.78	4.00	90.00	30.78	5.00	60.00	30.78
Model prediction (M)	5.16	19.26	25.22	4.96	50.28	20.22	5.49	20.50	24.76
% error	+29	−55	−18	+24	−44	−34	+10	−66	−20

diameter of the bead, X, is different. Since the flow rate is the same, the same values of δB and δA as derived in our first example were used in the model predictions. While the model predictions do not agree exactly with our observations, the predictive trend gives us confidence that the model is capable of refinement given more information of the adjustable parameters involved.

As the extrusion pressure is progressively decreased, the yield surfaces at $\xi_1 = \text{Bi}^{\text{A}}$ and $\xi_2 = \text{Bi}^{\text{B}}$ move closer to $\xi = X$ and $\xi = 1.0$, respectively. The boundary layer regions decrease in scale and both the flow rate and the shear stress on the interface decrease. In Figs. 20(a) and 20(b), we show the predicted bead spacing L_T and the bead length L_B as the pressure is changed. The axes of the graphs have been normalized with respect to a flow rate of $Q^* = 30.78\ \text{mm}^3/\text{s}$, where the expected values ΔP_f^*, L_T^* and L_B^* are approximately 46 bar, 60 mm, and 5 mm, respectively. At the lower critical pressure, $\text{Bi}^{\text{B}} \rightarrow 1.0$ (with $\text{Bi}^{\text{A}} < X$), and the outer region is no longer extruded; a thin core jet of material A is extruded from the center of the nozzle. At the upper critical pressure, $\text{Bi}^{\text{B}} \rightarrow X$ so that the entire outer annulus is yielded and extrudes continuously as a fluid layer. This large variation in the spacing L_T with a much weaker modulation in the bead length L_B is in good agreement with the data shown in Table V. The flow rate corresponding to Table V was half the flow rate in Table IV, and the extrusion pressure was recorded to be 8% lower at approximately 42 bar. Hence, the ratio $\Delta P_f/\Delta P_f^* = 0.92$. From Figs. 20(a) and 20(b), the model prediction of the most frequent L_T and L_B values corresponding to this lower flow rate is 112.8 and 5.4 mm, respectively, which agrees closely to the most frequent values reported in Table V. It appears clear that a simple model such as this can describe many of the gross features of the necklace instability.

V. DISCUSSION AND CONCLUSION

This paper has reported two different forms of extrusion instabilities observed during the cold extrusion of chocolate. In the first case, a stick–spurt instability has been observed. Both the magnitude of the associated pressure fluctuations and the form of the velocity fluctuations are easily monitored, and the fact that there are periods when there is no exit flow of chocolate while the extrusion piston is advancing, clearly demonstrates that the compressibility of the material is an important factor in the description of the instability. The value of the compressibility used in the modeling was assumed to be associated with that of the ''bulk'' chocolate, taking into account the possible presence of any gas voidage in the bed. We have also shown that the dynamics of the unstable chocolate extrusion can be described by incorporating compressibility plus a constitutive

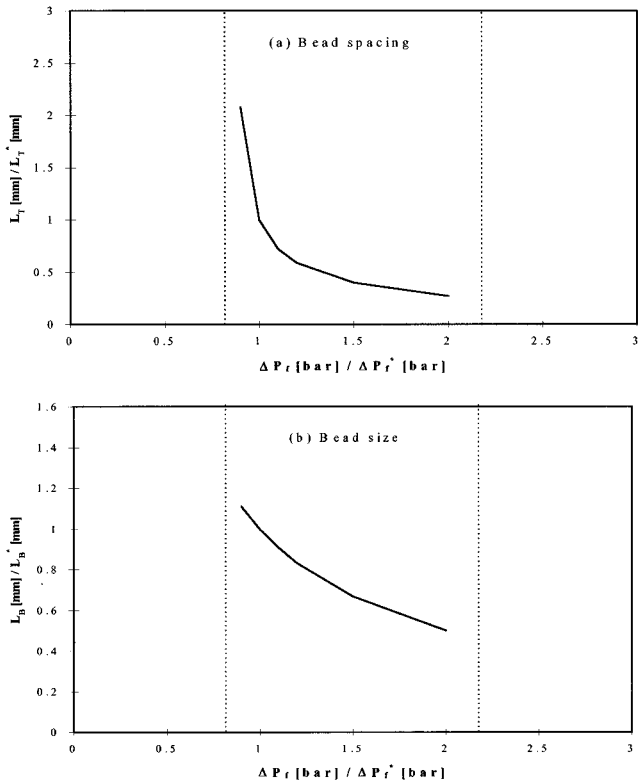

FIG. 20. Model prediction of effect of extrusion pressure on (a) bead spacing, L_T, and (b) bead size, L_B. Axes normalized with respect to a flow rate of $Q^* = 30.78\ \text{mm}^3/\text{s}$, where $\Delta P_f^* = 46$ bar, $L_T^* = 60$ mm (median value), and $L_B^* = 5$ mm (median value). Die = 4/4/45°, and $T = 22\ ^\circ\text{C}$.

response corresponding to a yield pressure, followed by a reduction, and then a shallow increase of flow pressure with extrusion flow rate. Adapting an analysis initially proposed by Weill (1980) and Molenaar and Koopmans (1994) for a viscous Newtonian liquid, we have shown that these two coupled features can describe, with the same accuracy, both the velocity and pressure fluctuations of the stick–spurt instability. Our description of the instability and the initial start-up conditions does not explicitly yield detailed information about, for example, wall boundary conditions; it does, however, require the material to have a representative value for bulk compressibility and it does require that the material have a yield pressure response followed by a flow pressure response similar to that given in Fig. 3. The importance of taking into account even small compressibility effects in describing instabilities of this class appear to be an essential feature if successful modeling is to be achieved.

The second type of instability that we have reported and modeled is concerned with the manufacture of the ''Ovaici necklace.'' This unusual instability occurred as a consequence of an unusual thermal history for loading the sample into the barrel of the extruder. A two-component chocolate system was formed with a high yield stress material near the wall encapsulating an inner core of chocolate characterized by a lower yield stress. We have successfully modeled to a first approximation the necklace formation by assuming that both phases extrude as a steady coannular flow of two Bingham-plastic materials. The inner core forms a central plug with a higher velocity than the outer

annulus. This inner core exerts a shear stress on the outer annulus, and when the net force exerted on the annulus exceeds the tensile yield strength of the annular chocolate, a necklace bead is formed. The effect is, therefore, generated by essentially steady flow in the extrusion capillary and the axial coextrusion of materials with different rheological responses. In our case, the difference in yield stress between the inner core and the necklace is the dominant factor and the reason for the striking appearance of the Ovaici necklace. It is our belief that this type of behavior could also occur in a less well-defined manner for certain polymer systems. The requirement for instability formation using this mechanism is that there is a rheological discontinuity in the material between the wall and the bulk of the material. This layer could be very small, and in some cases, of the order of microns. Wang and Drda (1996) discuss the possibility of a ''super fluid'' layer near the wall of a polyethylene melt flow and Brochard and de Gennes (1992) have indicated that the behavior of polymer chains near a wall can be expected to be different from the bulk. It is, therefore, plausible that the Ovaici necklace mechanism we have described in this paper may help our understanding of instabilities in other systems where, at present, the two-phase nature of the extrusion is not as clearly resolved as it is in the present material.

ACKNOWLEDGMENTS

The authors would like to thank Nestle York for their financial support during this project. In particular, the authors wish to thank Professor Peter Schroeder, Dr. Steve Beckett, and Mark Jury for their help and encouragement. A number of ideas described in this paper resulted from collaboration during the Isaac Newton Workshop on Complex Fluids held in Cambridge during 1996, and the authors would like to thank the organizers and sponsors of that Workshop for enabling us to benefit from this period of study.

APPENDIX

1. Derivation of velocity profiles for core–annular flow of two Bingham plastics coextruded in a circular die

The geometric configuration of the flow is given in Fig. 17. Component A flows axially in the core of the die and component B flows between the core and the inner wall. The *rheological assumptions* are that both fluids behave as Bingham plastics, hence, $\tau^{A} = \tau_y^{A} + \mu^{A}\,\dot{\gamma}$ and $\tau^{B} = \tau_y^{B} + \mu^{B}\dot{\gamma}$. The *boundary condition assumptions* are: (i) no slip at the wall, hence, at $\xi = 1.0$, $v_z^{B} = 0$; (ii) continuity of velocity and shear stress at the interface between components A and B, hence, at $\xi = X$, $v_z^{A} = v_z^{B}$; and (iii) zero shear stress at $r = 0$, hence, at $\xi = 0$, $\tau_{rz} = 0$. *Other assumptions* involved are: (i) fully developed incompressible, steady, isothermal pressure-driven flow; (ii) rectilinear flow with $P = P(z)$ only and $v = v_z(r)$ only; and (iii) uniform distributed yield material surfaces in the capillary section of the die. Applying the z component of the equation of motion in cylindrical coordinates for a fully developed pressure-driven flow, neglecting gravity effects and applying the assumptions stated above, the differential equation simplifies to

$$\tau_{rz} = -\frac{r\Delta P}{2L} = -\frac{r}{R}\frac{\Delta PR}{2L} = -\xi\frac{\Delta PR}{2L}, \tag{A1}$$

where $\Delta P = P_L - P_0$. Equation (A1) implies that there is a linearly increasing stress across the tube radius independent of fluid type or number. Also, at $r = R$, $\tau_{rz} = \tau_w$, hence,

$$\tau_w = +\frac{\Delta PR}{2L}. \tag{A2}$$

It can be observed that τ_{rz} and τ_w are linearly related as given by

$$\tau_{rz} = -\xi\tau_w. \tag{A3}$$

From this, the shear stress at the interface between materials A and B when flowing is given by

$$\tau_x = +X\tau_w. \tag{A4}$$

To compute velocity profiles $v_z^{\mathrm{A}}(r)$ and $v_z^{\mathrm{B}}(r)$, we need to evaluate whether the fluid has yielded. We define the dimensionless group ''Bingham number'' Bi as follows:

$$\mathrm{Bi} = \frac{\tau_y}{\tau_w}. \tag{A5}$$

When $\mathrm{Bi} = 0$, flow is Newtonian, when $0 < \mathrm{Bi} < 1.0$, there is a region of plug flow, and when $\mathrm{Bi} \geqslant 1.0$, there is no flow at all. For core–annular flow of two Bingham plastics, the location of the yield surfaces and the shape of the velocity profile depend on the relative values of the wall shear stress τ_w, the stress at the interface τ_x, and the yield stresses τ_y^{A}, τ_y^{B}. There are at least nine different configurations possible, which can be divided into two classes: (I) $\tau_y^{\mathrm{B}} > \tau_y^{\mathrm{A}}$ and (II) $\tau_y^{\mathrm{B}} < \tau_y^{A}$. Case (I) implies that outer fluid B yields first under some conditions, or inner fluid A yields first under some conditions, and case (II) implies that the outer fluid B always yields first. Case (I) is of direct interest to the formation of an Ovaici necklace and we do not consider case (II) further here. Within the case (I) type of motions, five distinct velocity profiles are possible depending on the wall shear stress as sketched in Fig. 21. As the wall shear stress increases, the Bingham number in each phase decreases and the velocity profiles change from 1A to 1B to 1C (depending on the ordering of τ_y^{A}, τ_y^{B}) and subsequently through 1D to 1E. In the limit, $\mathrm{Bi}^{\mathrm{A+B}} \to 0$ and the velocity profile approaches the core–annular flow of two Newtonian fluids, with a shape that depends on the ratio of $\mu^{\mathrm{B}}/\mu^{\mathrm{A}}$. We will consider the set of conditions where $0 < \mathrm{Bi}^{\mathrm{A}} < X < \mathrm{Bi}^{\mathrm{B}} < 1.0$. In this case, there are two regions of plug flow and two narrow ''boundary layers'' of viscous flow, as shown schematically in Fig. 18. The narrow ''boundary layers'' are regions of shearing deformation and is where the main resistance to flow occurs. At $\xi = \xi_1$, $\tau_{rz} = \tau_y^{\mathrm{A}}$, and material A yields. At $\xi = \xi_2$, $\tau_{rz} = \tau_y^{\mathrm{B}}$, and material B yields. ξ_1 and ξ_2 are the location of the interface between the yield and plug flow region for materials A and B, respectively. Their position can be evaluated from equating the equation for τ_{rz} with the equation used to describe the rheology of each component.

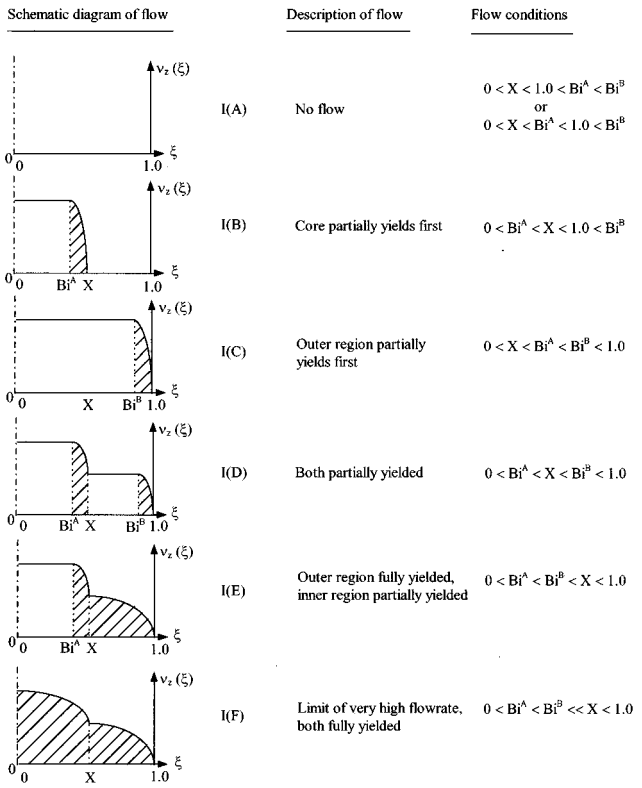

FIG. 21. Class I ($\tau_y^{\mathrm{A}} < \tau_y^{\mathrm{B}}$) motions of core–annular extrusion of Bingham plastics. As the flow rate is increased, the extrusion pressure ΔP_f rises and so does the wall shear stress τ_w. The schematic diagram of the flow pattern progression is then: I(A) → [I(B) or I(C)] → I(D) → I(E) → I(F).

Component B

$$\mu^{\mathrm{B}}\left(\frac{\partial v_z}{\partial r}\right)^{\mathrm{B}} - \tau_y^{\mathrm{B}} = -\xi\left(\frac{\Delta PR}{2L}\right), \tag{A6}$$

$$\text{at } \xi = \xi_2, \quad \left(\frac{\partial v_z}{\partial r}\right)^{\mathrm{B}} = 0, \tag{A7}$$

$$\therefore \xi_2 = \mathrm{Bi}^{\mathrm{B}}. \tag{A8}$$

Component A

$$\mu^{\mathrm{A}}\left(\frac{\partial v_z}{\partial r}\right)^{\mathrm{A}} - \tau_y^{\mathrm{A}} = -\xi\left(\frac{\Delta PR}{2L}\right), \tag{A9}$$

$$\text{at } \xi = \xi_1, \quad \left(\frac{\partial v_z}{\partial r}\right)^{\mathrm{A}} = 0, \tag{A10}$$

$$\therefore \xi_1 = \mathrm{Bi}^{\mathrm{A}}. \tag{A11}$$

2. Derivation of the velocity profiles

The flow across the circular die is divided into four regions; two regions of plug flow and two narrow ''boundary layers'' of viscous flow. There is no velocity gradient in the plug flow regions. We derive the equations giving the velocity profile in each region when flowing.

Component B

The velocity profile of material B in the zone $X \leqslant \xi \leqslant 1.0$ can be obtained by rearranging and integrating Eq. (A6) for v_z^{B} with respect to r (substituting $\xi = r/R$) and then applying the boundary condition of zero slip at the tube wall. This yields

$$v_z^{\mathrm{B}}(\xi) = \frac{\Delta P R^2}{4\mu^{\mathrm{B}} L}(1-\xi^2) - \frac{\tau_y^{\mathrm{B}} R}{\mu^{\mathrm{B}}}(1-\xi). \tag{A12}$$

The above expression is valid for $\xi_2 \leqslant \xi \leqslant 1.0$. For $X \leqslant \xi \leqslant \xi_2$ fluid B moves as a plug. To find the velocity of this plug, we evaluate expression (A12) at $\xi = \xi_2 = \mathrm{Bi}^{\mathrm{B}}$:

$$v_{\mathrm{plug}}^{\mathrm{B}} = \frac{\Delta P R^2}{4\mu^{\mathrm{B}} L}[1-(\mathrm{Bi}^{\mathrm{B}})^2] - \frac{\tau_y^{\mathrm{B}} R}{\mu^{\mathrm{B}}}(1-\mathrm{Bi}^{\mathrm{B}}). \tag{A13}$$

Factoring out

$$\frac{\Delta P R^2}{4\mu^{\mathrm{B}} L} = \left(\frac{\Delta P R}{2L}\right)\frac{R}{2\mu^{\mathrm{B}}} = \frac{\tau_w R}{2\mu^{\mathrm{B}}}$$

and substituting $\tau_y^{\mathrm{B}} = \mathrm{Bi}^{\mathrm{B}}\tau_w$ yields

$$v_{\mathrm{plug}}^{\mathrm{B}} = \frac{\tau_w R}{2\mu^{\mathrm{B}}}(1-\mathrm{Bi}^{\mathrm{B}})^2. \tag{A14}$$

This expression is valid for $X \leqslant \xi \leqslant \xi_2$.

Component A

The velocity profile of material A in the zone $0 \leqslant \xi \leqslant X$ can be obtained in a similar manner to that for material B. Rearranging and integrating Eq. (A9) for v_z^{A} with respect to r (substituting $\xi = r/R$) and applying the boundary condition of continuity of velocity at the interface between the two materials A and B, hence, at $\xi = X$, $v_z^{\mathrm{A}} = v_{\mathrm{plug}}^{\mathrm{B}}$, yields

$$v_z^{\mathrm{A}}(\xi) = v_{\mathrm{plug}}^{\mathrm{B}} + \frac{\Delta P R^2}{4\mu^{\mathrm{A}} L}(X^2-\xi^2) - \frac{\tau_y^{\mathrm{A}} R}{\mu^{\mathrm{A}}}(X-\xi). \tag{A15}$$

The above expression is valid for $\xi_1 \leqslant \xi \leqslant X$. For $0 \leqslant \xi \leqslant \xi_1$, material A moves as a plug. To find the velocity of this plug, we evaluate expression (A15) at $\xi = \xi_1 = \mathrm{Bi}^{\mathrm{A}}$:

$$v_{\mathrm{plug}}^{\mathrm{A}} = v_{\mathrm{plug}}^{\mathrm{B}} + \frac{\Delta P R^2}{4\mu^{\mathrm{A}} L}[X^2-(\mathrm{Bi}^{\mathrm{A}})^2] - \frac{\tau_y^{\mathrm{A}} R}{\mu^{\mathrm{A}}}(X-\mathrm{Bi}^{\mathrm{A}}). \tag{A16}$$

Factoring out

$$\frac{\Delta PR^2}{4\mu^{\mathrm{A}}L} = \left(\frac{\Delta PR}{2L}\right)\frac{R}{2\mu^{\mathrm{A}}} = \frac{\tau_w R}{2\mu^{\mathrm{A}}}$$

and substituting $\tau_y^{\mathrm{A}} = \mathrm{Bi}^{\mathrm{A}}\tau_w$ yields

$$v_{\mathrm{plug}}^{\mathrm{A}} = v_{\mathrm{plug}}^{\mathrm{B}} + \frac{\tau_w R}{2\mu^{\mathrm{A}}}(X - \mathrm{Bi}^{\mathrm{A}})^2. \tag{A17}$$

The above expression is valid for $0 \leqslant \xi \leqslant \xi_1$.

3. Derivation of total volumetric flow rate of two Bingham plastics coextruding in a core–annular configuration in a circular die, each with a region of yield and a region of plug flow

The velocity field can be integrated across the pipe and reexpressed in terms of the total volume flow rate. Equations (A12), (A14), (A15), and (A17) are each integrated with appropriate boundary conditions to find the volumetric flow for each region. The total flow rate is then the sum of the individual flow rates. Working in terms of r,

$$Q_{a-b} = \int_{r=a}^{r=b} v_z^{\mathrm{A,B}}(r)\,2\pi r\,dr, \tag{A18}$$

where $Q_{a\text{-}b}$ = volumetric flow rate between region a-b; $v_z^{\mathrm{A,B}}(r)$ = velocity profile of material A or B (in terms of r) through region a-b; a,b = boundary conditions. The total volume flow rate, Q_T, is calculated to be

$$Q_T = Q_{0-\xi_1} + Q_{\xi_1-X} + Q_{X-\xi_2} + Q_{\xi_2-1.0} = \frac{\tau_w R^3 \pi}{\mu^{\mathrm{B}}}\left(\frac{1}{4} - \frac{\mathrm{Bi}^{\mathrm{B}}}{3} + \frac{(\mathrm{Bi}^{\mathrm{B}})^4}{12}\right) + \frac{\tau_w R^3 \pi}{\mu^{\mathrm{A}}}\left(\frac{X^4}{4} - \frac{\mathrm{Bi}^{\mathrm{A}}X^3}{3} + \frac{(\mathrm{Bi}^{\mathrm{A}})^4}{12}\right). \tag{A19}$$

The above equation is also the *mass balance* equation.

References

AdewaleK. E. P. and A. I. Leonov, ''On modelling spurt flows of polymers,'' J. Non-Newtonian Fluid Mech. **49**, 133–138 (1993).

Adewale, K. E. P., O. Olabisi, A. A. Oyediran, and V. O. S. Olunloyo, ''A stick–slip problem related to melt fracture in polymer processing operations,'' Int. Polym. Process. VI **3**, 195–198 (1991).

Beaufils, P., B. Vergnes, and J. F. Agassard, ''Characterization of the sharkskin defect and its development with the flow conditions,'' Int. Polym. Process. IV **2**, 78–84 (1989).

Becker, J., P. Bengtsson, C. Klason, J. Kubat, and P. Saha, ''Pressure oscillations during capillary extrusion of high density polyethylene,'' Int. Polym. Process. VI **4**, 318–325 (1991).

Beckett, S. T., *Industrial Chocolate Manufacture and Use*, 2nd ed. (Blackie Academic & Professional, London/Glasgow, 1994).

Beckett, S. T., M. A. Craig, R. J. Gurney, B. S. Ingleby, M. R. Mackley, and T. C. L. Parsons, ''The cold extrusion of chocolate,'' Trans. IchemE **72**(C), 47–54 (1994).

Benbow, J. and J. Bridgwater, *Paste Flow and Extrusion* (Clarendon, Oxford, 1993).

Benbow, J. J. and P. Lamb, ''New aspects of melt fracture,'' SPE Trans. **3**, 7–17 (1963).

Brochard, F. and P. G. de Gennes, ''Shear dependent slippage at a polymer solid interface,'' Langmuir **8**, 3033–3037 (1992).

Chevalley, J., ''Rheology of Chocolate,'' J. Texture Studies **6**, 177–196 (1975).

Crook, S. J., ''The Cold Extrusion of Chocolate,'' Ph.D. thesis, Department of Chemical Engineering, The University of Cambridge (1997).

Dealy, J. M. and K. F. Wissbrun, *Melt Rheology and its Role in Plastics Processing: Theory and Applications* (Van Nostrand Reinhold, New York, 1990).

Firdaus, V. and P. P. Tong, ''Sharkskin melt fracture: effect on LLDPE film properties,'' J. Plastic Film Sheet. **8**, 333–340 (1992).

Georgiou, G. C. and M. J. Crochet, ''Time-dependent Compressible extrudate-swell problem with slip at the wall,'' J. Rheol. **38**, 1745–1755 (1994b).

Georgiou, G. C. and M. J. Crochet, ''Compressible viscous flow in slits with slip at the wall,'' J. Rheol. **38**, 639–654 (1994a).

Goddard, J., ''Perturbations and stability of motions with constant stretch histories,'' Proceedings of the XIIth International Congress on Rheology, Quebec City, Vol. 1, pp. 371–372 (1996).

Graham, M. D., ''Wall slip and the nonlinear dynamics of large amplitude oscillatory shear flows,'' J. Rheol. **39**, 697–712 (1995).

Holdsworth, S. D., ''Rheological models used for the prediction of the flow properties of food products: A literature review,'' Trans. IchemE **71**(C), 139–178 (1993).

Kolkka, R. W., D. S. Malkus, M. G. Hansen, G. R. Ierley, and R. A. Worthing, ''Spurt phenomena of the Johnson–Segalman fluid and related models,'' J. Non-Newtonian Fluid Mech. **29**, 303–335 (1988).

Larson, R. G., ''Instabilities in viscoelastic flows,'' Rheol. Acta **31**, 213–263 (1992).

Malkus, D. S., J. A. Nohel, and B. J. Plohr, ''Dynamics of shear flow of a non-Newtonian fluid,'' J. Comput. Phys. **87**, 464–487 (1990).

Molenaar, J. and R. J. Koopmans, ''Modelling polymer melt–flow instabilities,'' J. Rheol. **38**, 99–109 (1994).

Papanastasiou, T. C., ''Flows of materials with yield,'' J. Rheol. **31**, 385–404 (1987).

Pearson, J. R. A., ''Flow curves with a maximum,'' J. Rheol. **38**, 309–331 (1994).

Petrie C. J. S. and M. M. Denn, ''Instabilities in polymer processing,'' AIChE. J. **22**, 209–236 (1976).

Piau, J. M., N. E. Kissi, F. Toussaint, and A. Mezghani, ''Distortions of polymer melt extrudates and their elimination using slippery surfaces,'' Rheol. Acta **34**, 40–57 (1995).

Press, W. H., B. P. Flannery, S. A. Teukolsky, and W. T. Vetterling, *Numerical Recipes: The Art of Scientific Computing* (Cambridge University Press, Cambridge, 1986).

Sornberger, G., J. C. Quantin, R. Fajolle, B. Vergnes, and J. F. Agassant, ''Experimental study of the sharkskin defect in linear low density polyethylene,'' J. Non-Newtonian Fluid Mech. **23**, 123–135 (1987).

Wang, S. Q. and P. A. Drda, ''Superfluid-like stick–slip transition in capillary flow of linear Polyethylene melts. 1. General features,'' J. Am. Chem. Soc. **29**, 2627–2632 (1996).

Weill, A., ''Capillary flow of linear polyethylene melt: Sudden increase of flowrate,'' J. Non-Newtonian Fluid Mech. **7**, 303–314 (1980).